

Me 149

ACTA POLYTECHNICA SCANDINAVICA

MECHANICAL ENGINEERING SERIES No. 149

Developments in Turbulence Modelling with Reynolds-Averaged Navier–Stokes Equations

PATRIK RAUTAHEIMO

Helsinki University of Technology
Department of Mechanical Engineering
Laboratory of Applied Thermodynamics
FIN-02015 HUT
Finland

Dissertation for the degree of Doctor of Science in Technology to be presented with due permission of the Department of Mechanical Engineering, for public examination and debate in Auditorium K216 at Helsinki University of Technology (Espoo, Finland) on the 27th of April, 2001, at 12 noon.

ESPOO 2001

Rautaheimo, Patrik P. R., **Developments in Turbulence Modelling with Reynolds-Averaged Navier–Stokes Equations**. Acta Polytechnica Scandinavica, Mechanical Engineering Series No. 149, Espoo 2001, 65 pages. Published by the Finnish Academies of Technology, ISBN 951–666–569–1, ISSN 0001–687X, UDC 533.6.013.

Keywords: Turbulence modelling, Reynolds-stress model, finite volume method, parallel computing.

Abstract

The performance of different low-Reynolds number turbulence models applied to various flows is described. The emphasis is put on Chien's $k - \varepsilon$ model, an explicit algebraic Reynolds-stress model by Speziale *et al.*, and a full Reynolds-stress closure. The Reynolds-stress closure of this work has been developed by the author by combining different existing models.

Accurate numerical methods are developed to couple the momentum equations and the low-Reynolds number Reynolds-stress equations. Two methods are introduced and these vary depending on how much the source terms are taken into account implicitly. The production of turbulence can be used to couple the inviscid part of the momentum equations and the Reynolds-stress equations in the approximate Riemann solution.

As demanding problems are computed, it has been essential to parallelize the computer code. This has been performed via a message passing package. The code shows an excellent parallel performance even in the most complex topologies simulated.

In this thesis, validations are presented for ten different fluid dynamic problems. The test cases vary from a simple channel flow to complicated flows in rotating machinery. In the validations it is found that the Reynolds-stress closure generally performs better than the two-equation models in complex flows. Especially stream-line curvature is better captured by the Reynolds-stress closure. For the skin friction, the present Reynolds-stress closure does not give satisfactory results, and thus, some further development is needed. For simpler situations the two-equation models give comparable or even better results than the more complex models.

© All rights reserved. No part of the publication may be reproduced, stored in a retrieval system, or transmitted, in any form or by any means, electronic, mechanical, photocopying or otherwise, without the prior written permission of the author.

Foreword

This work has been carried out at the Laboratory of Applied Thermodynamics, Helsinki University of Technology, under the supervision of Professor Timo Siikonen. The research was a part of the Finnish National CFD Technology Programme 1995-1999, founded by the National Technology Agency (Tekes).

I would like to express my gratitude to Professor Timo Siikonen who has provided comments and discussions throughout my scientific work. He has given me guidance and provided an interesting and rich research topic. I am also grateful to all my colleagues for creating a friendly and challenging working environment. It has been a privilege to work with these people. I would especially like to express my gratitude to Esa Salminen, Antti Hellsten and Petri Kaurinkoski. Esa has made most of the computational grids used in this work, assisted me into the world of UNIX, and also corrected a lot of never-ending typing errors. Antti's research has been closely related to mine and thus, it has brought me a wider view to common research interests. Petri has supplied me with numerous problems and solutions pertaining to my work.

I express my thanks to all my friends who have provided unforgettable moments during sailing, skiing, cycling and other leisure time. Good friends are irreplaceable. I also express my deepest gratitude to my parents and sister for their support and encouragement through the years.

Espoo, May 2000

Patrik Rautaheimo

Contents

List of Publications	7
Nomenclature	9
1 Introduction	13
2 Modelling of a Fluid Flow	15
2.1 Navier–Stokes Equations	16
2.2 Reynolds-Averaged Navier–Stokes Equations	18
2.3 Turbulence Modelling	19
2.4 Low-Reynolds Number Models	23
3 Numerical Methods	27
3.1 Spatial Discretization	28
3.2 Diagonalization of the Flow Equations	30
3.3 Time Integration Method	33
3.4 Limitations of the Reynolds stresses	34
3.5 Parallel Computing	34
4 Validations	39
4.1 Channel Flow	39
4.2 Rotating Channel	40
4.3 Flat-Plate Boundary Layer	43
4.4 Wall Jet	43
4.5 Curved Duct	45
4.6 Surface-Mounted Cube	46
4.7 Matrix of Surface-Mounted Cubes	48
4.8 Return Channel	50
4.9 Centrifugal Compressor	53
4.10 Turbulent Mixing in the Core of a Nuclear Reactor	55
4.11 Improved Solid-Wall Boundary Treatment	56
4.12 Summary of the Validations	57
5 Conclusions	59
Bibliography	61

List of Publications

This thesis consists of an overview and the following publications.

1. P. Rautheimo, T. Siikonen and A. Hellsten, *Diagonalization of the Reynolds-Averaged Navier–Stokes Equations with the Reynolds-Stress Turbulence Model*, IMACS-COST Conference on Computational Fluid Dynamics, Lausanne, Switzerland, September 13-15, 1995.
2. P. Rautheimo and T. Siikonen, *Implementation of the Reynolds-stress Turbulence Model*, 3rd ECCOMAS Computational Fluid Dynamics Conference, Paris, France, September 9-13, 1996.
3. P. Rautheimo, E. Salminen and T. Siikonen, *Parallelization of a Multi-Block Navier-Stokes Solver*, 3rd ECCOMAS Computational Fluid Dynamics Conference, Paris, France, September 9-13, 1996.
4. P. Rautheimo and T. Siikonen, *Simulation of a Flow in a Return Channel with a Deswirl Cascade Using Advanced Turbulence Modelling*, 4th ECCOMAS Computational Fluid Dynamics Conference, Athens, Greece, September 7-11, 1998.
5. P. Rautheimo, E. Salminen and T. Siikonen, *Numerical Simulation of the flow in the NASA Low-Speed Centrifugal Compressor*, submitted to ASME Journal of Turbomachinery.
6. P. Rautheimo, E. Salminen, T. Siikonen and J. Hyvärinen, *Turbulent Mixing Between VVER-440 Fuel Bundle Subchannels: A CFD Study*, Proceedings of the 9th International Topical Meeting on Nuclear Reactor Thermal Hydraulics, San Francisco, California, October 3-8, 1999.
7. P. Rautheimo and T. Siikonen, *Improved Solid-Wall Boundary Treatment in Low-Reynolds Number Turbulence Models*, accepted for publication in AIAA Journal.

The author has carried the main responsibility for the research. He has performed all the theoretical development work, numerical simulations and analytical calculations in the included articles. He is also responsible for the writing of the Publications, except for Paper 3, in which the author has contributed actively to the writing process.

Nomenclature

A, B, C	Jacobian matrices of the flux vectors, $A = \partial F / \partial U$
CFL	Courant number
D	diffusion of the Reynolds stresses; wall correction in dissipation
E	total energy per unit volume
F, G, H	flux vectors in the x -, y - and z -directions
F	force
G	production of the kinetic energy of turbulence due to rotation
L	length; right eigenvector matrix with primitive variables
Ma	Mach number
Q	source-term vector
P	production of the kinetic energy of turbulence
Pr	Prandtl number
R	residual; right eigenvector matrix
Re	Reynolds number
Ro	rotation number, $Ro = 2\Omega h / U_b$
S	strain-rate tensor; area of cell face
T	temperature
Tu	turbulence intensity, $Tu = \sqrt{\frac{2}{3}k/U^2}$
U	vector of conservative variables; velocity
U_b	bulk velocity
V	volume; vector of primitive variables; velocity
W	vorticity-rate tensor
\mathcal{P}	relaxed pressure-strain tensor
\mathcal{T}	rotation operator
b_{ij}	anisotropy tensor, $b_{ij} = \widetilde{u_i'' u_j''} / (2k) - 1/3 \delta_{ij}$
c	model constant or function; speed of sound
c_f	skin-friction coefficient, $c_f = \tau_w / (1/2 \rho u_\infty^2)$
c_p	specific heat at a constant pressure
d	height of the cell
e	specific internal energy per unit volume
f	damping function
h	height
i, j, k	grid coordinate directions
k	kinetic energy of turbulence, $k = \widetilde{u_i'' u_i''} / 2$, heat conductivity
l	length scale
l_e	average size of energy-containing eddies

n_x, n_y, n_z	components of a unit normal vector
p	static pressure
q_i	heat flux in the i -direction
\vec{r}	location vector
t	time
u_i	velocity component in the i -direction
u, v, w	velocity components in the Cartesian coordinate system
\vec{v}	velocity vector
x, y, z	Cartesian coordinates
y_n	dimensional normal distance from the solid wall
$y_{1/2}$	jet-stream half-width
y^+	non-dimensional normal distance from the solid wall
Δ	difference operator
Φ	pressure-strain correlation
Ω	angular velocity
α	constant; angle of attack
δ_{ij}	Kronecker's delta
ε	dissipation of the kinetic energy of turbulence
ϵ_{ijk}	permutation tensor
η	Kolmogorov length scale
λ	eigenvalue
η	efficiency
μ	dynamic viscosity
ν	kinematic viscosity, $\nu = \mu/\rho$
ρ	density
σ	Schmidt's number
τ	shear-stress tensor
ϕ	scalar variable; part of the pressure-strain correlation
ω	turbulent vorticity, $\omega \propto \sqrt{k}/l$
ω_i	vorticity vector

Subscripts

T	turbulent conditions
b	bulk quantity
i	i -index; summation index
ij	ij -component of a matrix
i, j, k	grid coordinate directions
max	maximum value
m	meridional component
n	normal component
r	reference quantity
t	tangential component
v	viscous value
w	wall value

∞	free-stream value
x, y, z	component in the x -, y - and z -coordinate directions

Superscripts

T	transposition
l	left-hand quantity
r	right-hand quantity
\wedge	convective value
\sim	Favre time-averaging operator
$-$	time-averaging operator; mass flow averaging operator
\rightarrow	vector component
$''$	Favre-averaged fluctuating component
$'$	fluctuating component

1 Introduction

At the time of writing this, it is a dark and windy autumn night. Outside the wind is heavily shaking large trees and a great number of leaves have come loose. The leaves are flying in irregular paths, swirling all over. If one follows the effect of the wind longer, some large structures of motion can be distinguished, like a large number of leaves flying in circular paths. Suddenly, as fast as these large structures of motion appeared, they break up into smaller ones and vanish. The wind forces seem to be random, at least most of the time. Pick up one leaf and try to follow it. The motion of a single leaf appears to be unpredictable but still the leaves are being blown along in the wind and, finally, a large deposit of them can be found in some corners of the surrounding buildings. In this context, the motion of the leaves can be considered as a motion of air particles – following the leaves one can see turbulent flow paths. Turbulent flow paths are impossible to predict precisely, but if the motion is time averaged, the statistical methods can be used to make an attempt to predict the average movement of the leaves as well as that of the air particles. No analytical solution is available so a numerical approach must be used. Statistical methods and especially their numerical counterparts are the topic of this thesis.

Turbulence is something that takes place almost everywhere where fluid flows. It can be found in nature like in the atmosphere, in the currents of the sea, rivers and blood vessels. Most machines are also affected by turbulence, like all vehicles, engines, the ventilation of buildings and in the cooling of electronic components. To define turbulence is not an easy task, but perhaps the definition could be taken as given by Hinze [1]: “Turbulent fluid motion is an irregular condition of flow in which the various quantities show a random variation with time and space coordinates, so that statistically distinct average values can be discerned.”

The irregular motion is a very important feature of turbulence, since it enhances mixing. For example, the mixing brings high-speed fluid closer to the solid surface every now and then. This effect increases drag forces and it is often undesirable, as in all transport vehicles. Recently, a great deal of research has been carried out to decrease, e.g. the drag of an aircraft by reducing turbulent mixing next to the solid surfaces, since considerable savings could be achieved. Nevertheless, turbulence has also many desired effects. Without turbulent mixing the weather conditions on the earth would be much more violent, too hot in the equatorial area and too cold close to the poles, or, on a smaller scale, the cooling of an electronic component would be much harder. Turbulence increases heat transfer significantly in both examples. The irregular motion and random variation makes turbulence difficult to solve and model. However, models are needed in the engineering design calcu-

lations of the machines that are somehow related to fluid dynamics. Turbulence modelling plays a paramount role in computational fluid dynamics (CFD).

In this work, turbulent flows are simulated by one of the modern numerical methods. Because the turbulent flow is highly irregular and, thus, impossible to simulate directly using direct numerical simulation (DNS) in most cases, the statistical approach has been used. This makes it possible to resolve complex problems. In the statistical approach, turbulent forces are taken into account by the Reynolds stresses. There are no closed-form equations for the Reynolds stresses and they must be modelled to some degree. This work concentrates on a comparison between different classical approaches, a two-equation model, an explicit algebraic Reynolds-stress model and a full Reynolds-stress model. The problem with the linear two-equation models is that they do not take into account the effect of the streamline curvature and they assume the Reynolds-stress tensor to be aligned with the strain-rate tensor. With these limitations it is not possible to simulate some of the turbulence-driven phenomena, e.g. a secondary flow in a square duct. Anisotropic alternatives such as the Reynolds-stress models offer the potential to forecast also these kind of phenomena. The use of the Reynolds-stress models for complex flows is not yet well documented. For complex flows there have been only a few validations for the Reynolds-stress closures in the literature and, consequently, here the focus is on the Reynolds-stress model. New numerical methods are introduced to couple the Reynolds-stress and flow equations. The capability of the different turbulence models is found out by validation cases.

Computational fluid dynamics demands large computing resources. The lack of computer resources is always a problem in fluid dynamics. Although the single processor performance has increased rapidly, it does not fulfil the requirements of solving large fluid dynamic problems, and therefore the problems have to be parallelized in order to utilize the present computers efficiently. In this work, the code has been parallelized using a most portable and very efficient alternative, message passing. Parallel performance shows excellent efficiency even with the most complicated problems tested.

In the following, a short description of fluid flows, especially turbulent flows is given. Firstly, emphasis is placed upon the problems encountered when solving these equations numerically. After this, the models to represent turbulent forces are described. Both isotropic and anisotropic alternatives are applied. None of the methods employed in this work utilize the law of the wall, and consequently, they can be used in complex situations. The numerical and computational issues are also considered in this thesis. This overview lays stress on validation, the details of the models can be found in publications. Validation of the models is carried out with ten test problems that range from simple two-dimensional cases to complex rotating three-dimensional flows. Finally, conclusions from the methods and the test cases are drawn.

2 Modelling of a Fluid Flow

Fluid flows can be categorized in many ways. One of the principal divisions is between laminar and turbulent flows. In a laminar flow the fluid paths are regular and smooth. Laminar flow can be steady or unsteady. Turbulent flow is characterized by irregular flow paths and it is always unsteady. Laminar flow becomes unstable when one of the problem characteristic parameters, Reynolds number, Grashof number, Taylor number, Richardson number, increases above some critical values. Generally, only the Reynolds number is important and thus, it is considered here. If the Reynolds number is increased from the critical value, the flow becomes turbulent. The Reynolds number can be considered as a ratio between the convective and viscous forces as

$$Re = \frac{F_{\text{conv}}}{F_{\text{vis}}} = \frac{\rho_r U_r^2}{\mu_r \frac{U_r}{L_r}} = \frac{\rho_r U_r L_r}{\mu_r} \quad (2.1)$$

where ρ_r , U_r , μ_r and L_r are reference density, velocity, molecular viscosity and length, respectively. The Reynolds number can be also considered as a ratio of a problem length scale L_r and viscosity length scale $\mu_r/(\rho_r U_r)$. The value of the critical Reynolds number varies with different flows.

In a turbulent flow, swirls or eddies of a different size are present. The largest eddies arise from the velocity difference between the flow layers, for example close to the solid surfaces or between two jets. Larger eddies break up into smaller ones. Finally, due to the viscosity, the smallest eddies dissipate to heat. A size ratio of the smallest and the largest eddies can be large. This ratio depends on the Reynolds number as well as on a particular flow. The smallest eddies are of the size of the Kolmogorov length scale

$$\eta = (\nu^3/\varepsilon)^{1/4} \quad (2.2)$$

in which $\nu = \mu/\rho$ is the kinematic viscosity and ε is the dissipation of turbulent kinetic energy. Here, it is assumed that the flow field can be divided into two parts as $u = \bar{u} + u'$, averaged velocity and turbulent fluctuation. Turbulent kinetic energy is defined as the energy of the fluctuating velocity. After the eddies have broken up into the size of the Kolmogorov length scale they dissipate to heat. Dissipation can be expressed as

$$\varepsilon = A u'^3/l_e \quad (2.3)$$

where A is a constant of the order of unity, u' is the fluctuation velocity and l_e is an average size of the energy-containing eddies. Using these equations, the ratio l_e/η

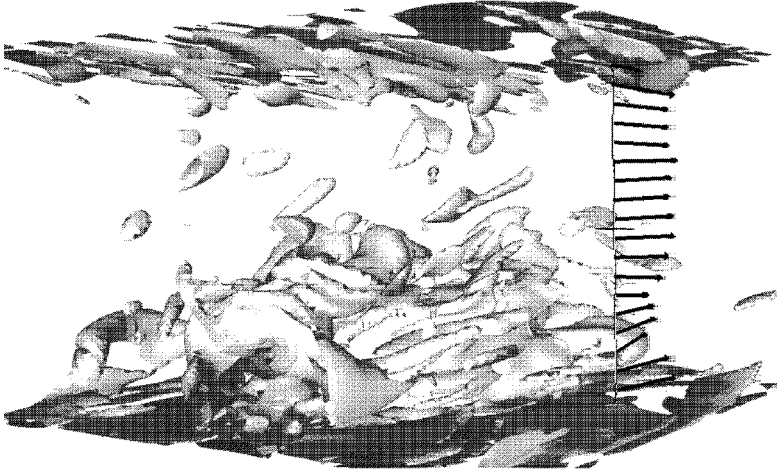


Fig. 2.1: Cross-flow vorticity iso-surfaces $\left(\sqrt{\omega_x^2 + \omega_y^2}\right)$ in the flow over a matrix of cubes in a channel. The cube is located at the centre of the bottom wall behind the iso-surfaces. The results are from DNS. More details of the test case can be found in Section 4.7.

can be solved

$$l_e/\eta = A^{1/4} (l_e u'/\nu)^{3/4} \quad (2.4)$$

Generally, it can be approximated that $l_e \propto L_r$ and $u' \propto U_r$ leading to a ratio between the reference length and the smallest eddies

$$L_r/\eta \propto Re^{3/4} \quad (2.5)$$

In engineering applications, the Reynolds number is typically from 10^5 to 10^8 . This means that the ratio of scales varies between 10^4 to 10^6 . To resolve all the scales, the number of the computational points in every coordinate direction has to be of the same order as the ratio of the scales.

In order to get an insight of the complexity of turbulent flow, an instantaneous vorticity iso-surface in the matrix of cubes in a channel is shown in Fig. 2.1. There is a cube located at the centre of the bottom wall. It can be seen that the vorticity is increased at the vicinity of the cube. At the ceiling, typical turbulent streaks can be seen. The flow is unsteady and very irregular, as can be seen in the velocity vectors at the right-hand side of the figure.

Next, the flow equations are described, the statistical approach to simulate turbulent flows is introduced, and the modelling of the effects of turbulence is presented.

2.1 Navier–Stokes Equations

The Navier–Stokes equations describe fluid flow. They comprise five partial differential equations, one for the conservation of mass, three for the conservation of momentum and one for the conservation of energy. The momentum equation can

be written in a rotating coordinate system with absolute velocities as

$$\frac{\partial}{\partial t}(\rho u_i) + \frac{\partial}{\partial x_k}(\rho u_i \hat{u}_k) = -\frac{\partial p}{\partial x_i} + \frac{\partial \tau_{ik}}{\partial x_k} - \left(\rho \vec{\Omega} \times \vec{v} \right)_i \quad (2.6)$$

where u_i is the i :th component of the instantaneous velocity, $\vec{\Omega}$ is the angular velocity vector, \vec{v} is the velocity vector, τ is the shear-stress tensor and \hat{u} is a convective velocity defined by

$$\hat{u}_i = u_i - \left(\vec{\Omega} \times \vec{r} \right)_i \quad (2.7)$$

Here \vec{r} is a position vector (origin at the rotation axis). The last term in Eq. (2.6) comes from the rotating coordinate system that is applied frequently in this work. To ensure the conservation of mass and energy, the continuity equation and the energy equation are written as

$$\frac{\partial \rho}{\partial t} + \frac{\partial \rho \hat{u}_i}{\partial x_i} = 0 \quad (2.8)$$

$$\frac{\partial E}{\partial t} + \frac{\partial}{\partial x_i} [E \hat{u}_i + p u_i] = \frac{\partial}{\partial x_i} [u_j \tau_{ij} - q_i] \quad (2.9)$$

where the total internal energy is $E = \rho e + \rho \frac{u_i u_i}{2}$, e is the specific internal energy, q_i is the component of the heat flux. For a Newtonian fluid, the viscous stress tensor is

$$\tau_{ij} = \mu \left[\frac{\partial u_j}{\partial x_i} + \frac{\partial u_i}{\partial x_j} - \frac{2}{3} \frac{\partial u_k}{\partial x_k} \delta_{ij} \right] \quad (2.10)$$

In this work, all fluids are considered to be Newtonian. Fourier's law is used for the heat flux

$$q_i = -k \frac{\partial T}{\partial x_i} \quad (2.11)$$

In order to close the system, the equation of state specifies the relationship between the thermodynamic variables: pressure p , density ρ and internal energy e . Viscosity μ and heat conductivity k can be functions of temperature T and pressure p . Here, μ and k are calculated from Sutherland's formula, which is only a function of temperature.

The above equations can be used to solve all type of flows, including turbulent ones. There are a few analytical solutions for the Navier–Stokes equations in laminar flows [2]. For turbulent flow, no analytical solutions are known but fortunately the modern computer can be used to solve Navier–Stokes equations numerically. A problem arises with the large ratio of scales that leads to a large number of grid points. The number of grid points must be at least L_r/η in each coordinate direction in order to describe all the scales. Since the time-step size is proportional to the grid size, the cost of simulation scales as

$$\text{Cost of Simulation} \propto (L_r/\eta)^4 \propto Re^3 \quad (2.12)$$

where the ratio of scales L_r/η is taken from Eq. (2.5). The cost of the simulation rises rapidly with the Reynolds number. To get more perspective, a fluid flow in

a channel is studied. In the well-known channel flow by Kim *et al.* [3] 250 CPU hours of the CRAY-XMP was used with $Re_H \approx 6\,000$. At present this problem could be solved with the most powerful computer available in Finland (January 1, 2000, SGI Origin2000 with 128 R12k) roughly 170 times faster in the optimum case. With the Origin2000, 1.5 hours would be sufficient to solve the problem. According to Eq. (2.12) the channel flow with $Re_H \approx 15\,000$ could be simulated in 24 hours. However, in engineering flows the Reynolds number is generally 100 or 1 000 times larger and thus, according to Eq. (2.12), roughly 10^6 to 10^9 days would be needed with the present supercomputers to solve practical cases. If it is assumed that the computing power will double every 1.5 years, which is rather optimistic, the problem with $Re_H \approx 1.5 \cdot 10^6$ will be solved in 24 hours approximately in the year 2030, and $Re_H \approx 15 \cdot 10^6$ in the year 2045.

Direct solving of the Navier–Stokes equations is called Direct Numerical Simulation (DNS). As was shown with the channel flow example, it is not feasible with existing computers in the near future. This has led to different types of methods to make the Navier–Stokes equations less sensitive to the different size of the scales. Below is a list of the most popular methods presented

- Direct Numerical Simulation (DNS)
- Large Eddy Simulation (LES)
- Reynolds-averaged Navier–Stokes (RANS) simulations

The first one, DNS, does not include any modelling, as mentioned earlier. In the second one, LES, the small eddies are described by a model and the large eddies are solved directly. In the third approach, one dimension, more precisely, the time dimension is averaged. These equations are called Reynolds-averaged Navier–Stokes (RANS) equations. This approach is, strictly speaking, valid only where a steady averaged flow can be distinguished. However, the same method is generally used for transient problems.

2.2 Reynolds-Averaged Navier–Stokes Equations

The Navier–Stokes equations can be averaged with respect to time in order to avoid the simulation of small scale fluctuations. The variables are divided into a time-averaged part and a fluctuating part. Here, a mass weighted, i.e. Favre-averaging [4], is used

$$f = \tilde{f} + f'' \quad (2.13)$$

where

$$\tilde{f} = \frac{\overline{\rho f}}{\bar{\rho}} \quad (2.14)$$

The overline operator is defined as

$$\bar{f} = \frac{1}{\Delta t} \int_{t_0}^{t_0 + \Delta t} f \, dt \quad (2.15)$$

where Δt is large compared to the time-scale of the turbulent fluctuation and small compared to the large-scale unsteadiness. In some cases, this requirement may not be valid. It must be noted that in this way the time averages of the fluctuating quantities are not equal to zero, in general, unless $\rho' = 0$. Instead, the time average of the doubly primed fluctuation multiplied by the density is equal to zero

$$\overline{\rho f''} = 0 \quad (2.16)$$

By substituting Eq. (2.13) into the momentum equations (2.6) and taking a time average over the equations we obtain

$$\frac{\partial}{\partial t}(\bar{\rho}\tilde{u}_i) + \frac{\partial}{\partial x_k}(\bar{\rho}\tilde{u}_i\tilde{u}_k) = -\frac{\partial \bar{p}}{\partial x_i} + \frac{\partial}{\partial x_k}(\bar{\tau}_{ik} - \overline{\rho u_i'' u_k''}) - \left(\bar{\rho}\vec{\Omega} \times \vec{v}\right)_i \quad (2.17)$$

where, ignoring viscosity fluctuations, the viscous stress tensor is

$$\tau_{ij} = \mu \left[\frac{\partial \tilde{u}_j}{\partial x_i} + \frac{\partial \tilde{u}_i}{\partial x_j} - \frac{2}{3} \frac{\partial \tilde{u}_k}{\partial x_k} \delta_{ij} \right] + \mu \left[\frac{\partial \overline{u_j''}}{\partial x_i} + \frac{\partial \overline{u_i''}}{\partial x_j} - \frac{2}{3} \frac{\partial \overline{u_k''}}{\partial x_k} \delta_{ij} \right] \quad (2.18)$$

The time-averaged momentum equation is very similar to the instantaneous momentum equation (2.6). The viscous stress tensor gets a more complicated form. In practice, the viscous terms involving the doubly primed fluctuations are expected to be small, and based on order of magnitude arguments [5] are potential candidates for being ignored. If the doubly primed fluctuations in Eq. (2.18) are ignored, only one new term is introduced into the momentum equation, the Reynolds-stress component $\overline{\rho u_i'' u_j''}$.

A similar procedure as for the momentum equations is applied also for the continuity (2.8) and the energy equation (2.9), after which a complete set of RANS equations is obtained.

2.3 Turbulence Modelling

By applying the time-averaging procedure, the small-scale fluctuations are avoided. However, new terms, the Reynolds stresses, are introduced into the momentum equations. Also in the energy equation, similar expressions containing the effect of temperature fluctuation are present. In this work, these are taken into account by a simple eddy-viscosity assumption [6], and are not studied in the following. Hence, the main emphasis is put on momentum equations. Turbulence modelling with RANS equations can be divided into three different approaches. In the first one, the differential equations for every component of the Reynolds stresses $\overline{\rho u_i'' u_j''}$ are obtained and solved. In the second one, the differential and algebraic equations are used to describe turbulent forces. In the third one, Reynolds stresses are assumed to depend locally on some algebraic expression of velocities, its derivatives and perhaps also on wall distance and some condition at the wall. The second alternative uses features from the first and the third approach and is called here the reduced differential model.

Reynolds-Stress Equations

The equation for the Reynolds stresses can be derived by using the momentum equation. After some manipulation [7, 8] the following equations are obtained

$$\begin{aligned} \frac{\partial \overline{\rho u_i'' u_j''}}{\partial t} + \frac{\partial (\overline{\rho \tilde{u}_k u_i'' u_j''})}{\partial x_k} = & - \left[\overline{\rho u_i'' u_k''} \frac{\partial \tilde{u}_j}{\partial x_k} + \overline{\rho u_j'' u_k''} \frac{\partial \tilde{u}_i}{\partial x_k} \right] + \overline{p' \left(\frac{\partial u_j''}{\partial x_i} + \frac{\partial u_i''}{\partial x_j} \right)} \\ & - \frac{\partial}{\partial x_k} \left[\overline{\rho u_i'' u_j'' u_k''} + \delta_{ik} \overline{p' u_j''} + \delta_{jk} \overline{p' u_i''} - (\tau_{ik} u_j'' + \tau_{jk} u_i'') \right] \\ & - \left(\tau_{ik} \frac{\partial u_j''}{\partial x_k} + \tau_{jk} \frac{\partial u_i''}{\partial x_k} \right) - \left(\overline{u_i''} \frac{\partial \bar{p}}{\partial x_j} + \overline{u_j''} \frac{\partial \bar{p}}{\partial x_i} \right) \\ & + \epsilon_{jkl} \Omega_k \overline{\rho u_i'' u_l''} + \epsilon_{ikl} \Omega_k \overline{\rho u_j'' u_l''} \end{aligned} \quad (2.19)$$

where the left-hand side contains the time derivative and the convection term; the right-hand side, the production P_{ij} , the pressure-strain term Φ_{ij} , the diffusion D_{ij} , the dissipation ε_{ij} , the mean pressure-gradient term $-\overline{u_i''} \partial \bar{p} / \partial x_j - \overline{u_j''} \partial \bar{p} / \partial x_i$, and the production due to the system rotation G_{ij} .

Assuming nearly incompressible flow, the mean pressure-gradient term can be ignored, and the Reynolds-stress model (RSM) can be written in the following simplified form [7]

$$\frac{\partial \overline{\rho u_i'' u_j''}}{\partial t} + \frac{\partial (\overline{\rho \tilde{u}_k u_i'' u_j''})}{\partial x_k} = P_{ij} + \Phi_{ij} + D_{ij} - \rho \varepsilon_{ij} + G_{ij} \quad (2.20)$$

The production and the rotation terms are exact

$$P_{ij} = - \left[\overline{\rho u_i'' u_k''} \frac{\partial \tilde{u}_j}{\partial x_k} + \overline{\rho u_j'' u_k''} \frac{\partial \tilde{u}_i}{\partial x_k} \right] \quad (2.21)$$

$$G_{ij} = \epsilon_{jkl} \Omega_k \overline{\rho u_i'' u_l''} + \epsilon_{ikl} \Omega_k \overline{\rho u_j'' u_l''} \quad (2.22)$$

As a weak compressibility is assumed, the molecular diffusion can be approximated as

$$(\tau_{ik} u_j'' + \tau_{jk} u_i'') \approx \mu \frac{\partial \widetilde{u_i'' u_j''}}{\partial x_k} \quad (2.23)$$

and the diffusion term obtains the form

$$D_{ij} = - \frac{\partial}{\partial x_k} \left[\overline{\rho u_i'' u_j'' u_k''} + \delta_{ik} \overline{p' u_j''} + \delta_{jk} \overline{p' u_i''} - \mu \frac{\partial \widetilde{u_i'' u_j''}}{\partial x_k} \right] \quad (2.24)$$

where pressure diffusion $(\delta_{ik} \overline{p' u_j''} + \delta_{jk} \overline{p' u_i''})$ is usually ignored. With a weak compressibility assumption also the dissipation gets a simpler form

$$\bar{\rho} \varepsilon_{ij} = \left(\overline{\tau_{ik} \frac{\partial u_j''}{\partial x_k}} + \overline{\tau_{jk} \frac{\partial u_i''}{\partial x_k}} \right) \approx 2\mu \frac{\partial u_i''}{\partial x_k} \frac{\partial u_j''}{\partial x_k} \quad (2.25)$$

Although, the dissipation rate gets a simpler form, it must be modelled as well as the pressure strain Φ_{ij} .

Algebraic Models

This group of models is one of the most popular methods to describe the Reynolds stresses. The most widely used assumption is that the Reynolds-stress tensor depends linearly on the strain-rate tensor

$$S_{ij} = \frac{1}{2} \left(\frac{\partial \tilde{u}_j}{\partial x_i} + \frac{\partial \tilde{u}_i}{\partial x_j} \right) \quad (2.26)$$

and the turbulent forces act in a similar way as viscous forces in momentum equation. This idea was presented as early as in 1877 by Boussinesq

$$-\overline{\rho u_i'' u_j''} = \mu_T \left(2S_{ij} - \frac{2}{3} \frac{\partial \tilde{u}_k}{\partial x_k} \delta_{ij} \right) - \frac{2}{3} \bar{\rho} k \delta_{ij}. \quad (2.27)$$

This expression is also called the eddy-viscosity assumption. Here, two new terms are introduced, the eddy viscosity μ_T and the kinetic energy of turbulence, $k = \frac{1}{2} \overline{u_i'' u_i''}$. Eddy viscosity (also called turbulent viscosity) can be defined in different ways. Dimensionally, it depends on the turbulent velocity and length scales. If \sqrt{k} is the turbulent characteristic velocity scale, the eddy viscosity can be written as

$$\mu_T = \bar{\rho} \sqrt{k} l \quad (2.28)$$

where l is a length scale that characterizes the size of the largest turbulent eddies. If both scales are taken from an algebraic equation, as in the well-known Baldwin-Lomax model [9], the third approach is used. These models are usually robust. The disadvantages of the algebraic models is that they are valid only for some particular flows. They cannot simulate separations correctly, for example.

Reduced Differential Models

Since the full RSM is many times too complex and algebraic models are not generally valid, differential models are developed which do not have differential equations for each Reynolds stress separately. Basically, the reduced differential models are very similar to the algebraic models. They use generally the same eddy viscosity assumption Eq. (2.27). Reduced differential models differ from algebraic models such that the velocity and length scales are determined by some differential equations. Many variants of these models have been presented and only the most popular are presented here. The most common way to describe the turbulence is by using the $k - \varepsilon$ model [10–12]. In this approach, turbulent viscosity is described by using the kinetic energy of turbulence k , and dissipation of turbulent kinetic energy ε as

$$\mu_T = \bar{\rho} \sqrt{k} l = c_\mu \bar{\rho} \sqrt{k} k^{3/2} / \varepsilon = c_\mu \bar{\rho} \frac{k^2}{\varepsilon} \quad (2.29)$$

in which ε is defined as $\varepsilon = \frac{1}{2} \overline{\varepsilon_{ii}} = \overline{\tau_{kl} / \bar{\rho} \partial u_k'' / \partial x_l}$ and c_μ is a model constant or function. For k and ε , the differential transport equations can be obtained. The

equation for kinetic energy of turbulence $k = \frac{1}{2} \widetilde{u_i'' u_i''}$ can be obtained by taking a half of the trace of the Reynolds-stress Eqs. (2.19)

$$\begin{aligned} \frac{\partial}{\partial t}(\bar{\rho}k) + \frac{\partial}{\partial x_i}(\bar{\rho} \tilde{u}_i k) = & -\overline{\rho u_i'' u_j''} \frac{\partial \tilde{u}_i}{\partial x_j} - \frac{\partial}{\partial x_i} \left(\bar{\rho} \widetilde{k u_i''} + \overline{p' u_i''} - \overline{u_k'' \tau_{ki}} \right) \\ & + \overline{p' \frac{\partial u_k''}{\partial x_k}} - \overline{u_k'' \frac{\partial \bar{p}}{\partial x_k}} - \overline{\tau_{ki} \frac{\partial u_k''}{\partial x_i}} \end{aligned} \quad (2.30)$$

An exact equation for the dissipation could be also obtained, but the result will be complicated and quite useless for computation. The equation for the dissipation, as well as for other possible length-scale parameters, is based on a similar convection-diffusion equation with source and sink as the equation of turbulent kinetic energy k . For the dissipation of turbulent kinetic energy, this is usually written as

$$\frac{\partial}{\partial t}(\bar{\rho}\varepsilon) + \frac{\partial}{\partial x_i}(\bar{\rho} \tilde{u}_i \varepsilon) = \frac{\varepsilon}{k} (c_{\varepsilon 1} P - c_{\varepsilon 2} \bar{\rho} \varepsilon) - \frac{\partial}{\partial x_i} \left(\bar{\rho} \widetilde{\varepsilon u_i''} + \mu \frac{\partial \varepsilon}{\partial x_i} \right) \quad (2.31)$$

where $c_{\varepsilon 1}$ and $c_{\varepsilon 2}$ are model constants or functions. Similar equations can also be presented with various other length-scale measuring parameters, like the $k - \omega$ models ($\omega \propto \sqrt{k}/l$) [13], which have recently been gaining in popularity. It must be remembered that the length-scale equations are always more or less of an “*ad hoc*” nature and tuning the model constants is based on some simplified flows or just on trial and error.

Lately, it has been found that the linear approximation may not be sufficient for the Reynolds stresses Eq. (2.27). In the eddy-viscosity assumption, the Reynolds stresses are considered to be a function of k, ε (or other length-scale parameter), and the strain-rate tensor S_{ij} . In these more advanced approaches, the Reynolds stresses are also functions of the vorticity-rate tensor W_{ij}

$$W_{ij} = \frac{1}{2} \left(\frac{\partial \tilde{u}_i}{\partial x_j} - \frac{\partial \tilde{u}_j}{\partial x_i} \right) \quad (2.32)$$

Thus, a general higher-order dependency from the vorticity- and strain-rate tensors can be written as

$$\overline{\rho u_i'' u_j''} = f(\rho, k, \varepsilon, S_{kl}, W_{kl}, i, j) \quad (2.33)$$

In the most commonly used approach to get these relations, the convection of the Reynolds-stress anisotropy tensor b_{ij} is assumed to be zero

$$\frac{\partial b_{ij}}{\partial t} + \frac{\partial u_k b_{ij}}{\partial x_k} = 0 \quad (2.34)$$

The anisotropy tensor is defined as

$$b_{ij} = \frac{\widetilde{u_i'' u_j''}}{2k} - \frac{1}{3} \delta_{ij} \quad (2.35)$$

For two-dimensional flows, the Reynolds-stress anisotropy tensor can be assumed to be a function of the strain-rate, vorticity-rate tensors and turbulent time-scale k/ε [14, 15]

$$b_{ij} = b_{ij}(k/\varepsilon, S_{kl}, W_{kl}) \quad (2.36)$$

This function is only valid for two-dimensional mean flows but, in general, it is used for three-dimensional flows as well.

2.4 Low-Reynolds Number Models

Turbulence models for the RANS equations are divided into low- and high-Reynolds number models. In high-Reynolds number models the flow is not solved next to the solid surfaces and wall functions are used. This means that boundary conditions can be applied to points in the flow field next to the solid surfaces. This procedure can be applied for situations in which the universal wall functions are valid. However, the wall functions describe the flow accurately only for a flat-plate boundary layer with a zero or constant pressure gradient and thus, for complex flow situations, the calculation should be extended onto the solid boundaries. This can be done if low-Reynolds number turbulence models are used.

In this thesis, many low-Reynolds number models are used. Three of them are used in most of the problems. The first one is Chien's $k - \varepsilon$ model [16] (CH). This model was already available in the CFD code at the beginning of this work and is applied as a base-line model throughout the work. The numerical implementation of this approach is described by Siikonen [6]. The second one is an explicit algebraic Reynolds-stress model (EARSIM) by Gatski *et al.* [14] (GS). The implementation of this is described in Paper 4. The third one is a full Reynolds-stress closure. The model combines the work of Chien [16], Shima [17] and Speziale *et al.* [18] and it is described in detail in Papers 4 and 5. It is referred to in this work as RSM and the numerical implementation is given in Papers 1 and 2. Here, a short description of the various turbulence closures mentioned above is given.

Two-equation Models

Models based on the solution of k - and ε -equations can be written in a general form as [19]

$$\mu_T = c_\mu f_\mu \bar{\rho} \frac{k^2}{\tilde{\varepsilon}} \quad (2.37)$$

$$\varepsilon = \tilde{\varepsilon} + D \quad (2.38)$$

$$\frac{\partial}{\partial t}(\bar{\rho}k) + \frac{\partial}{\partial x_i}(\bar{\rho}\hat{u}_i k) = \frac{\partial}{\partial x_i} \left[(\mu + \mu_T/\sigma_k) \frac{\partial k}{\partial x_i} \right] + P - \bar{\rho}\varepsilon \quad (2.39)$$

$$\begin{aligned} \frac{\partial}{\partial t}(\bar{\rho}\tilde{\varepsilon}) + \frac{\partial}{\partial x_i}(\bar{\rho}\hat{u}_i \tilde{\varepsilon}) &= \frac{\partial}{\partial x_i} \left[(\mu + \mu_T/\sigma_\varepsilon) \frac{\partial \tilde{\varepsilon}}{\partial x_i} \right] + c_{\varepsilon 1} \frac{\tilde{\varepsilon}}{k} P \\ &\quad - c_{\varepsilon 2} f_2 \frac{\bar{\rho}\tilde{\varepsilon}^2}{k} + E \end{aligned} \quad (2.40)$$

Table 2.1 summarizes functions and constants for the different two-equation turbulence models applied in this study. The production of turbulent kinetic energy P is

Table 2.1: Functions and constants for the two-equation turbulence models.

Model	D	c_μ	$c_{\varepsilon 1}$	$c_{\varepsilon 2}$	σ_k	σ_ε
CH	$2\nu k/y_n^2$	0.09	1.44	1.92	1.0	1.3
GS	0	0.088	1.39	1.83	1.0	1.3

Model	f_μ	f_2	E
CH	$1 - e^{-0.0115y^+}$	$1 - 0.22e^{-Re_T^2/36}$	$-2\mu(\tilde{\varepsilon}/y_n^2)e^{-0.5y^+}$
GS	1	$1 - e^{-Re_y/12.5}$	0

written without additional modelling as

$$P = -\overline{\rho u_i'' u_j''} \frac{\partial \tilde{u}_i}{\partial x_j} \quad (2.41)$$

where the Reynolds stresses $\overline{\rho u_i'' u_j''}$ are obtained in the CH model by using the eddy-viscosity assumption Eq. (2.27)

$$\overline{\rho u_i'' u_j''} = -2\mu_T S_{ij} + \frac{2}{3} \delta_{ij} \bar{\rho} k \quad (2.42)$$

In the GS model the Reynolds stresses are explicit functions of the mean strain rate and the vorticity tensor as

$$\begin{aligned} \overline{\rho u_i'' u_j''} = & \frac{2}{3} \bar{\rho} k \delta_{ij} - \frac{6(1 + \eta^2) \alpha_1}{3 + \eta^2 + 6\xi^2 \eta^2 + 6\xi^2} \bar{\rho} \frac{k^2}{\varepsilon} \\ & \left[(S_{ij} - \frac{1}{3} S_{kk} \delta_{ij}) + \alpha_4 \frac{k}{\varepsilon} (S_{ik} W_{kj}^* + S_{jk} W_{ki}^*) \right. \\ & \left. - \alpha_5 \frac{k}{\varepsilon} (S_{ik} S_{kj} - \frac{1}{3} S_{kl} S_{kl} \delta_{ij}) \right] \end{aligned} \quad (2.43)$$

where

$$W_{ij}^* = W_{ij} - \frac{2}{C_4 - 2} \epsilon_{mji} \Omega_m \quad (2.44)$$

Above, the modified vorticity tensor comes from the production due to the system rotation. Unfortunately, this violates coordinate frame invariance, and thus, caution should be used if it is applied with rotating coordinate systems. In Eq. (2.43) η and ξ are strain-rate invariants defined by

$$\eta = \frac{1}{2} \frac{\alpha_3}{\alpha_1} (S_{ij} S_{ij})^{\frac{1}{2}} \frac{k}{\varepsilon} \quad \xi = \frac{1}{2} \frac{\alpha_2}{\alpha_1} (W_{ij}^* W_{ij}^*)^{\frac{1}{2}} \frac{k}{\varepsilon} \quad (2.45)$$

Above, α_1 , α_2 , α_3 , α_4 and α_5 are parameters with the following definitions [20]

$$\begin{aligned} \alpha_1 &= (\frac{4}{3} - C_2)g/2 & \alpha_2 &= (2 - C_3)^2 g^2/4 \\ \alpha_3 &= (2 - C_4)^2 g^2/4 & \alpha_4 &= (2 - C_4)g/2 \\ \alpha_5 &= (2 - C_3)g & g &= 1/(C_1 + C_5 - 1) \end{aligned} \quad (2.46)$$

where the constants of the pressure-strain model of Speziale *et al.* [18] are applied

$$\begin{aligned} C_1 &= 3.4 & C_2 &= 0.36 & C_3 &= 1.25 \\ C_4 &= 0.4 & C_5 &= 1.88 \end{aligned} \quad (2.47)$$

Reynolds-stress Model

Here Eq. (2.20) for the Reynolds stresses is rewritten as

$$\frac{\partial \overline{\rho u_i'' u_j''}}{\partial t} + \frac{\partial (\bar{\rho} \hat{u}_k \widetilde{u_i'' u_j''})}{\partial x_k} = P_{ij} + \Phi_{ij} + D_{ij} - \rho \varepsilon_{ij} + G_{ij}. \quad (2.48)$$

In this equation, the production and the rotation terms are exact, whereas the turbulent diffusion, the pressure strain and the dissipation rate must be modelled. In this work the high-Reynolds number modelling developed by Speziale, Sarkar and Gatski (SSG) [18] is applied for the pressure strain Φ_{ij} . The low-Reynolds number counterpart is based on Shima's work [17]. The connection of the low- and the high-Reynolds number regions is done by using a wall distance dependent damping function. The dissipation transport equation is based on Chien's $k - \varepsilon$ model.

In the low-Reynolds number model, the pressure-strain and the dissipation rate terms can be connected as [17]

$$\begin{aligned} p' \left(\frac{\partial u_i''}{\partial x_j} + \frac{\partial u_j''}{\partial x_i} \right) - 2\mu \frac{\partial u_i''}{\partial x_k} \frac{\partial u_j''}{\partial x_k} &= \Phi_{ij} - \rho \varepsilon_{ij} = \\ \phi_{ij,1} + \phi_{ij,2} + \phi_{ij,w} - \frac{2}{3} \delta_{ij} \bar{\rho} \varepsilon & \end{aligned} \quad (2.49)$$

where $\phi_{ij,1}$ represents the fluctuation part of Φ_{ij} and the anisotropic part of ε_{ij} , $\phi_{ij,2}$ is the mean-strain part of Φ_{ij} , and $\phi_{ij,w}$ takes into account the wall proximity effects. These terms are modelled in the following way [17, 18]

$$\begin{aligned} \phi_{ij,1} &= - [\bar{C}_1 - (\bar{C}_1 - 2)f_{w,1}] \bar{\rho} \varepsilon b_{ij} \\ &\quad + C_2 (1 - f_{w,1}) \bar{\rho} \varepsilon (b_{ik} b_{kj} - \frac{1}{3} \Pi \delta_{ij}) \end{aligned} \quad (2.50)$$

$$\begin{aligned} \phi_{ij,2} &= (C_3 - C_3^* \Pi^{1/2}) \bar{\rho} k S_{ij} + \\ &\quad C_4 \bar{\rho} k (b_{ik} S_{jk} + b_{jk} S_{ik} - \frac{2}{3} b_{kl} S_{kl} \delta_{ij}) + \\ &\quad C_5 \bar{\rho} k (b_{ik} W_{jk} + b_{jk} W_{ik}) \end{aligned} \quad (2.51)$$

$$\begin{aligned} \phi_{ij,w} &= \left[\alpha \left(P_{ij} - \frac{2}{3} \delta_{ij} P \right) + \gamma \bar{\rho} k S_{ij} + \right. \\ &\quad \left. \beta \left(D_{ij} - \frac{2}{3} \delta_{ij} P \right) \right] f_{w,1} \end{aligned} \quad (2.52)$$

where P_{ij} is the production from Eq. (2.21) and $P = \frac{1}{2} P_{ii}$ from Eq. (2.41). The tensor D_{ij} and the wall damping function $f_{w,1}$ are defined as

$$D_{ij} = - \left[\overline{\rho u_i'' u_k''} \frac{\partial \tilde{u}_k}{\partial x_j} + \overline{\rho u_j'' u_k''} \frac{\partial \tilde{u}_k}{\partial x_i} \right] \quad (2.53)$$

$$f_{w,1} = \exp \left[- \left(0.011 \bar{\rho} \sqrt{k} y_n / \mu \right)^4 \right] \quad (2.54)$$

Table 2.2: Constants in the pressure-strain term.

Model	C_1	C_1^*	C_2	C_3	C_3^*	C_4	C_5
LRR	3.0	0.0	0.0	0.8	0.0	1.75	1.31
SSG	3.4	1.80	4.2	0.8	1.30	1.25	0.40

The anisotropy tensor b_{ij} , second invariant of the anisotropy tensor Π , and model parameter \bar{C}_1 are

$$b_{ij} = \frac{\widetilde{u_i'' u_j''}}{2k} - \frac{1}{3} \delta_{ij} \quad \Pi = b_{kl} b_{kl} \quad \bar{C}_1 = C_1 + C_1^* P / (\bar{\rho} \varepsilon) \quad (2.55)$$

Here Eqs. (2.50 - 2.52) are written in a general form. Different models can be obtained by changing the constants. The idea is that the constants of Launder *et al.* [21] (LRR) with Shima's low-Reynolds number part are used close to the wall, and the SSG model constants are applied far away from the wall. For example, C_1 is not a constant, but it is a combination of two model parameters

$$C_1 = f_{w,2} C_{1,LRR} + (1 - f_{w,2}) C_{1,SSG} \quad (2.56)$$

The same treatment is done also for C_1^* , C_2 , C_3 , C_3^* , C_4 and C_5 . The constants for the different models are given in Table 2.2. The wall correction values, α , β and γ , and the wall damping function $f_{w,2}$ were assigned after test calculations with a simple channel flow as

$$\alpha = 0.45 \quad \beta = 0 \quad \gamma = 0.04 \quad (2.57)$$

$$f_{w,2} = \exp \left[- \left(0.015 \bar{\rho} \sqrt{k} y_n / \mu \right)^4 \right] \quad (2.58)$$

During this work, the constant γ was found to have a strong effect on the skin friction. With a value of $\gamma = 0.04$, the skin friction is systematically overpredicted. In most of the test cases, if γ is set to 0.055, the prediction of skin friction is improved. Consequently, only for the channel flow $\gamma = 0.04$ is used, but for the rest of the cases the value of $\gamma = 0.055$ is applied.

Complex geometries often contain corners. The effect of the corners is described by multiplying locally the effects of the walls

$$f_w = 1 - (1 - f_{w,i-dir})(1 - f_{w,j-dir})(1 - f_{w,k-dir}). \quad (2.59)$$

For the diffusion term D_{ij} a simple scalar model [22] is applied

$$D_{ij} = \frac{\partial}{\partial x_k} \left[(\mu + \mu_T / \sigma_{ij,T}) \frac{\partial \widetilde{u_i'' u_j''}}{\partial x_k} \right] \quad (2.60)$$

where the turbulent eddy viscosity μ_T is calculated as in Eq. (2.37) for the CH model, and the appropriate Schmidt number is set to $\sigma_{ij,T} = 1.0$.

3 Numerical Methods

In this chapter, the numerical methods are summarized. The focus is on the convection-diffusion equations with the source terms and it is applied to solve the Reynolds-stress equations. Also, the methods to take account of the effect of the Reynolds stresses in the momentum equation are studied. These methods are applied to various turbulence quantity equations. The summary of parallelization is also presented with a parallel efficiency investigation. Details of numerical methods can be found in Papers 1 and 2. A complete description of the parallel solution is given in Paper 3.

Recent progress in computer technology has made it possible to numerically simulate complex flows. Reynolds-averaged equations can be used to solve flows around various geometries. However, complex geometries and the nonlinear turbulence models make numerical solutions a difficult task. In this work, the physics and the numerics have been separated and a common paradigm

$$[\text{NUMERICS}] \Delta U = \text{PHYSICS} \quad (3.1)$$

is used. The right-hand side of the equations must be solved with high accuracy, whereas the left-hand side should ensure the stability and good convergence.

In recent years, a lot of development work has been done in order to couple the Reynolds-averaged Navier–Stokes equations (RANS) and turbulence models. With algebraic turbulence modelling, the numerical methods remain essentially the same as in a laminar flow. Difficulties arise as more advanced methods, like two-equation models, are used. The implementation of the Reynolds-stress turbulence model in the curvilinear coordinate system is a demanding task, see e.g. [23]. The difficulties include the robustness and efficiency of the numerical scheme as well as the complexity of the computer code. This complexity may cause coding errors and reduce the efficiency.

If the performance of the flow solver is needed to run an order of magnitude faster than in a conventional algorithm, then parallel processing must be considered. For over a decade there have been parallel computers and networks of computers that can be used to run single work in several processors. Naturally, this places special requirements on the algorithms. The basic idea behind the parallelization is that the computing work is divided into smaller subtasks. Each subtask is solved in a different processor. Usually this requires essential changes in the algorithms.

The implementation of the Reynolds-stress model in an existing multi-block Navier–Stokes solver [24] is performed in this thesis. In order to minimize the

coding errors, a Cartesian form of the fluxes is utilized for the inviscid terms and for the Reynolds stresses. This is accomplished by applying suitable rotation operators. The flow equations are solved using Roe's flux-difference splitting [25]. In incompressible flow, a pseudo-compressibility approach [26] with a Roe-type damping term can be applied. For the spatial discretization, a MUSCL-type TVD-scheme to approximate convective volume-face fluxes is applied. The discretized equations are integrated in time by applying the DDADI factorization [27]. In order to increase the convergence speed, the multigrid method is applied [28]. In the multigrid method, the flow is also solved for a coarser grid or grids in order to rapidly damp large oscillation that might occur during the iteration. It does not have any effect on the final solution. The computational domain is divided into different blocks. This makes it possible to simulate more complex geometries and it is also used in parallelization.

In order to increase the robustness and accuracy of the method, the RANS equations and the Reynolds-stress equations are coupled in the approximate Riemann solution. Two coupling methods between the RANS equations and the equations for the Reynolds stresses have been developed in Papers 1 and 2.

3.1 Spatial Discretization

In the CFD code used [6], a finite-volume technique is applied. The RANS equations have an integral form

$$\frac{d}{dt} \int_V U dV + \int_S \vec{F}(U) \cdot d\vec{S} = \int_V Q dV \quad (3.2)$$

for an arbitrary fixed region V with a boundary S . Here U is vector of conservative variables, F is the flux vector and Q is a vector of source terms. Performing the integrations for a computational cell i yields

$$V_i \frac{dU_i}{dt} = - \sum_{\text{faces}} S \hat{F} + V_i Q_i \quad (3.3)$$

where the sum is taken over the faces of the computational cell. The flux for the face is defined as

$$\hat{F} = n_x(F - F_\nu) + n_y(G - G_\nu) + n_z(H - H_\nu) \quad (3.4)$$

where F , G , H , F_ν , G_ν and H_ν are the inviscid and viscid fluxes in the x -, y - and z -directions, respectively. For the RANS equations (2.17) with the equations for turbulent kinetic energy k , dissipation ε and scalar variable ϕ , fluxes F and F_ν can

be written as

$$F = \begin{pmatrix} \rho \hat{u} \\ \rho u \hat{u} + p + \overline{\rho u'' u''} \\ \rho v \hat{u} + \overline{\rho u'' v''} \\ \rho w \hat{u} + \overline{\rho u'' w''} \\ E \hat{u} + p u + \overline{\rho u'' u''} u + \overline{\rho u'' v''} v + \overline{\rho u'' w''} w \\ \rho k \hat{u} \\ \rho \tilde{\varepsilon} \hat{u} \\ \rho \phi \hat{u} \end{pmatrix}, \quad F_v = \begin{pmatrix} 0 \\ \tau_{xx} \\ \tau_{xy} \\ \tau_{xz} \\ u(\tau_{xx} + \frac{2}{3}\rho k) + v\tau_{xy} + w\tau_{xz} - q_x \\ \mu_k(\partial k / \partial x) \\ \mu_\varepsilon(\partial \tilde{\varepsilon} / \partial x) \\ \mu_\phi(\partial \phi / \partial x) \end{pmatrix}, \quad (3.5)$$

where the viscous stress tensor is defined in Eq. (2.18). Here, the time-averaging operators (bars and tildes) are not written for simplicity. The Reynolds stresses can be taken into account in inviscid or viscid fluxes. Here, these are included in the inviscid flux but a more detailed study is provided in the following section. The heat flux contains a laminar and a turbulent part, and is written as

$$\vec{q} = -(k + k_T) \nabla T = - \left(\mu \frac{c_p}{Pr} + \mu_T \frac{c_p}{Pr_T} \right) \nabla T \quad (3.6)$$

where k_T is turbulent heat conductivity and Pr_T a turbulent Prandtl number. The diffusion coefficients of the turbulence quantities and the scalar quantity are approximated as

$$\mu_k = \mu + \frac{\mu_T}{\sigma_k} \quad \mu_\varepsilon = \mu + \frac{\mu_T}{\sigma_\varepsilon} \quad \mu_\phi = \mu + \frac{\mu_T}{\sigma_\phi} \quad (3.7)$$

where σ_k , σ_ε and σ_ϕ are the appropriate Schmidt's numbers and the turbulent viscosity μ_T is determined by the turbulence model.

In the evaluation of the inviscid fluxes, Roe's method [25] is applied. A rotation operator is used for the velocity components as well as for the Reynolds stresses. The flux is calculated as

$$\hat{F} = \mathcal{T}^{-1} F(\mathcal{T}U). \quad (3.8)$$

where \mathcal{T} is a rotation operator that transforms the dependent variables to a local coordinate system normal to the cell surface. In this way, programming is greatly enhanced, since only the Cartesian form of the inviscid flux F is needed. This is calculated from

$$F(U^l, U^r) = \frac{1}{2} [F(U^l) + F(U^r)] - \frac{1}{2} \sum_{k=1}^K r^{(k)} |\lambda^{(k)}| \alpha^{(k)} \quad (3.9)$$

where U^l and U^r are the solution vectors evaluated on the left and right sides of the cell surface, $r^{(k)}$ is a the right eigenvector of the Jacobian matrix $A = \partial F / \partial U$, the corresponding eigenvalue is $\lambda^{(k)}$, and $\alpha^{(k)}$ is the corresponding characteristic variable obtained from $R^{-1} \delta U$, where $\delta U = U^r - U^l$. A MUSCL-type discretization is used for the evaluation of U^l and U^r . In the evaluation of U^l and U^r , primitive variables (ρ, u, v, w, p), and conservative turbulent variables ($\rho k, \overline{\rho u_i'' u_j''}, \rho \tilde{\varepsilon}$) are utilized. Primitive variables are used in order to obtain smooth distributions for the primitive variables through boundary layers. For the turbulence quantities, the second-order upwind scheme with the limiter of van Albada *et al.* [29] is used. The use of the limiter for the turbulence quantities was found to be important, especially at the edge of the turbulent boundary layer. In this region, e.g. k and ε go rapidly from finite values to zero, and thus, overshoots might occur. The Jacobian matrix A can be split in the usual way

$$A = R \Lambda R^{-1} = M L \Lambda L^{-1} M^{-1}. \quad (3.10)$$

where R and R^{-1} are the right and left eigenvector matrices of A ; L and L^{-1} are the corresponding matrices with respect to the primitive variables, Λ is the diagonal eigenvalue matrix, and M and M^{-1} are the transformation matrices between the conservative and the primitive variables.

3.2 Diagonalization of the Flow Equations

Coupling between the Reynolds-averaged Navier–Stokes equations and turbulence models can enhance the convergence and stability. In this work, new methods to take account of the Reynolds stresses in the momentum equation are introduced in Papers 1 and 2. As the Reynolds-stress model is applied, the Reynolds stresses may be connected with the pressure [7]. In the i -momentum equation, the resulting effective anisotropic pressure can be defined as

$$p_i^* = p + \overline{\rho u_i'' u_i''} \quad (3.11)$$

Note that in this way the effective pressure is direction dependent. In order to utilize Roe's method, the Jacobian of the flux vectors must be diagonalized. This requires that the Jacobian matrix of the flux vector has a complete set of eigenvectors. Unfortunately, linearly independent eigenvectors cannot be found if the anisotropic pressure field of Eq. (3.11) is applied. In the case of a $k - \varepsilon$ model with an isotropic pressure field, linearly independent eigenvectors exist [6]. Since the anisotropic pressure field is difficult to handle, the turbulent pressure can be approximated by the mean of the three components

$$p^* = p + \frac{2}{3} \rho k \quad (3.12)$$

Using this, the flux vector can be divided into isotropic and anisotropic parts, and the Jacobian of the isotropic part can be diagonalized.

The second method of diagonalization utilizes the production of the turbulence P_{ij} in vector F . The production term is exact in RSM and it can be included in vector F . In this way, independent eigenvectors can be found. Next, both of the diagonalization approaches are described.

Isotropic Diagonalization

Vector F defined by Eq. (3.5) can be divided into two parts

$$F = F_1 + F_2 \quad (3.13)$$

where vector F_1 corresponds to the isotropic part of turbulence and F_2 contains the anisotropic part.

$$F_1 = \begin{pmatrix} \rho \hat{u} \\ \rho u \hat{u} + p + \frac{2}{3} \rho k \\ \rho v \hat{u} \\ \rho w \hat{u} \\ E \hat{u} + p u + \frac{2}{3} \rho k u \\ \frac{\rho u_i'' u_j'' \hat{u}}{\rho \tilde{\epsilon} \hat{u}} \end{pmatrix}, F_2 = \begin{pmatrix} 0 \\ \overline{\rho u'' u''} - \frac{2}{3} \rho k \\ \frac{\rho u'' v''}{\rho u'' w''} \\ (\overline{\rho u'' u''} - \frac{2}{3} \rho k) u + \overline{\rho u'' v'' v} + \overline{\rho u'' w'' w} \\ 0 \\ 0 \end{pmatrix} \quad (3.14)$$

The Jacobian of the vector F_1 can be diagonalized similarly to that of the $k - \epsilon$ model [6]. Vector F_2 can be evaluated using central differences. In this approach the Reynolds stresses are not rotated, instead \hat{F}_2 is calculated directly from Eq. (3.4)

$$\hat{F}_2 = \begin{pmatrix} 0 \\ n_x (\overline{\rho u'' u''} - \frac{2}{3} \rho k) + n_y \overline{\rho u'' v''} + n_z \overline{\rho u'' w''} \\ n_x \overline{\rho u'' v''} + n_y (\overline{\rho v'' v''} - \frac{2}{3} \rho k) + n_z \overline{\rho v'' w''} \\ n_x \overline{\rho u'' w''} + n_y \overline{\rho v'' w''} + n_z (\overline{\rho w'' w''} - \frac{2}{3} \rho k) \\ \hat{f}_{2,2} u + \hat{f}_{2,3} v + \hat{f}_{2,4} w \\ 0 \\ 0 \end{pmatrix} \quad (3.15)$$

where $\hat{f}_{2,i}$ is i :th element of the vector \hat{F}_2 .

Anisotropic Diagonalization

As mentioned earlier, linearly independent eigenvectors cannot be found if the anisotropic pressure field of Eq. (3.11) is applied. However, the production term introduced coupling between the velocity field and the Reynolds stresses. The production term is exact in RSM and it can be separated from the other source terms

$$Q = Q' + P \quad (3.16)$$

Production is included in vector F . This is not a conservative form of the vector F but RSM is never in a conservative form because of the source terms.

Usually the Jacobian takes the simplest form if the primitive variables are used. Here, the selected primitive variables are

$$V = (\rho \quad u \quad v \quad w \quad e \quad \widetilde{u''u''} \quad \widetilde{u''v''} \quad \widetilde{u''w''} \quad \widetilde{v''v''} \quad \widetilde{v''w''} \quad \widetilde{w''w''} \quad \varepsilon)^T \quad (3.17)$$

After some mathematical manipulation, the Jacobian $(\partial F / \partial U)$ can be obtained in the primitive variable form as

$$A' = \begin{pmatrix} u & \rho & 0 & 0 & 0 & 0 & 0 & 0 & 0 & 0 & 0 & 0 \\ \frac{p_e}{\rho} + \frac{\widetilde{u''u''}}{\rho} & u & 0 & 0 & \frac{p_e}{\rho} & 1 & 0 & 0 & 0 & 0 & 0 & 0 \\ \frac{\widetilde{u''v''}}{\rho} & 0 & u & 0 & 0 & 0 & 1 & 0 & 0 & 0 & 0 & 0 \\ \frac{\widetilde{u''w''}}{\rho} & 0 & 0 & u & 0 & 0 & 0 & 1 & 0 & 0 & 0 & 0 \\ \frac{p}{\rho} & \frac{p}{\rho} & 0 & 0 & u & 0 & 0 & 0 & 0 & 0 & 0 & 0 \\ 0 & 2 \frac{\widetilde{u''u''}}{\rho} & 0 & 0 & 0 & u & 0 & 0 & 0 & 0 & 0 & 0 \\ 0 & \frac{\widetilde{u''v''}}{\rho} & \frac{\widetilde{u''u''}}{\rho} & 0 & 0 & 0 & u & 0 & 0 & 0 & 0 & 0 \\ 0 & \frac{\widetilde{u''w''}}{\rho} & 0 & \frac{\widetilde{u''u''}}{\rho} & 0 & 0 & 0 & u & 0 & 0 & 0 & 0 \\ 0 & 0 & 2 \frac{\widetilde{u''v''}}{\rho} & 0 & 0 & 0 & 0 & 0 & u & 0 & 0 & 0 \\ 0 & 0 & \frac{\widetilde{u''w''}}{\rho} & \frac{\widetilde{u''v''}}{\rho} & 0 & 0 & 0 & 0 & 0 & u & 0 & 0 \\ 0 & 0 & 0 & 2 \frac{\widetilde{u''w''}}{\rho} & 0 & 0 & 0 & 0 & 0 & 0 & u & 0 \\ 0 & 0 & 0 & 0 & 0 & 0 & 0 & 0 & 0 & 0 & 0 & u \end{pmatrix} \quad (3.18)$$

It can be seen that there are extra terms in the lower left and upper right corners. The left one is the effect of the velocities on the Reynolds-stress equations, and the right one is the effect of the Reynolds stresses on the momentum equations. In this case the eigenvalues, i.e. the characteristic speeds, are

$$\lambda^{(i)} = u, u + c, u - \sqrt{\widetilde{u''u''}}, u - \sqrt{\widetilde{u''u''}}, u - c, u, u + \sqrt{\widetilde{u''u''}}, u + \sqrt{\widetilde{u''u''}}, u, u, u, u \quad (3.19)$$

where c is the speed of sound. For an arbitrary equation of state, the speed of sound is

$$c^2 = p_e p / \rho^2 + p_\rho + 3 \widetilde{u''u''} \quad (3.20)$$

Notations p_e and p_ρ are

$$p_e = \left. \frac{\partial p}{\partial e} \right|_\rho \quad p_\rho = \left. \frac{\partial p}{\partial \rho} \right|_e \quad (3.21)$$

It can be seen that the Reynolds stresses have an effect on the characteristic speeds and on the definition of the speed of sound. The speed of sound is direction dependent, although the effect is larger only in very high velocity flows.

Using the primitive variables, the characteristic variables are obtained from

$$\delta W = (\alpha^{(i)}) = L^{-1} \delta V = R^{-1} \delta U \quad (3.22)$$

where $\delta V = V^r - V^l$. The matrices L^{-1} and R get a rather complex form and can be found in [30].

3.3 Time Integration Method

The discretized equations are integrated in time by applying the DDADI factorization [27]. This is based on the approximate factorization and on the splitting of the Jacobians of the flux terms. In the implicit stage the factorization is done isotropically. The implicit stage consists of a backward and forward sweep in every coordinate direction. The sweeps are based on a first-order upwind differencing. In addition, the linearization of the source term is factored out of the spatial sweeps. The boundary conditions are treated explicitly, and a spatially varying time-step is utilized. The implicit stage can be written after factorization as follows

$$\begin{aligned}
 & \left[I + \frac{\Delta t}{V_i} (\partial_i^- S_{i+1/2} A_i^+ - \partial_i^+ S_{i-1/2} A_i^-) \right] \times \\
 & \left[I + \frac{\Delta t}{V_j} (\partial_j^- S_{j+1/2} B_j^+ - \partial_j^+ S_{j-1/2} B_j^-) \right] \times \\
 & \left[I + \frac{\Delta t}{V_k} (\partial_k^- S_{k+1/2} C_k^+ - \partial_k^+ S_{k-1/2} C_k^-) \right] \times \\
 & \quad \left[I - \Delta t D_i \right] \Delta U_i = \frac{\Delta t}{V_i} R_i
 \end{aligned} \tag{3.23}$$

where $\partial_{i,j,k}^-$ and $\partial_{i,j,k}^+$ are first-order spatial difference operators in the i -, j - and k -directions, A , B and C are the corresponding Jacobian matrices, $D = \partial Q / \partial U$, and R_i is the right-hand side of Eq. (3.3). The Jacobians are calculated as

$$A^\pm = R(|\Lambda^\pm| + kI)R^{-1} \tag{3.24}$$

where Λ^\pm are diagonal matrices containing the positive and negative eigenvalues, and k is a factor to ensure the stability of the viscous term [31]

$$k = \frac{2(\mu + \mu_T)}{\rho d} \tag{3.25}$$

where d is the height of the cell. The idea of the diagonally dominant factorization is to put as much weight on the diagonal as possible. In the i -direction the tridiagonal equation set resulting from Eq. (3.23) is replaced by two bidiagonal sweeps and a matrix multiplication [6].

It can be seen that Eq. (3.23) has the same form as Eq. (3.1); the numerics are on the left-hand side and physics, the explicit residual R_i , on the right-hand side. Here the turbulent viscosity is also used for the Reynolds-stress calculations to stabilize the solution. According to Eq. (3.1), it will not change the results, but it will improve the convergence. In this way, the implicit stage can be kept simpler than taking the Reynolds stresses implicitly into account. The scheme is even numerically more robust without highly nonlinear relations to the Reynolds stresses. The turbulent viscosity μ_T is always calculated from Eq. (2.37) by using Chien's model. Also tests were done to directly calculate the turbulent viscosity from the eddy-viscosity assumption (2.27) but it did not work as robustly as the Chien's expression.

To take account of the effect of the source terms implicitly might be a complicated task. This is especially true for the Reynolds-stress model with low-Reynolds number extension. The previously developed method [6] to take account of arbitrary source terms is adopted with small changes. Details of the method are given in Paper 2. The basic idea is that the effect of the source term is limited by the value of the solved variable. The maximum change of U caused by source term Q is limited to $|\Delta U_{\max}|$. The value of $|\Delta U_{\max}|$ is evaluated using the current values of $\overline{\rho u_i'' u_j''}$ as

$$|\Delta(\overline{\rho u_i'' u_j''})_{\max}| = C_{k,1} |\overline{\rho u_i'' u_j''}| + C_{k,2}(1 - \delta_{ij}) \frac{2}{3} \bar{\rho} k \quad (3.26)$$

where $C_{k,1}$ and $C_{k,2}$ were set to 0.2 and 0.02 after the test calculations. The second term in Eq. (3.26) ensures a possible change of sign in the off-diagonal components of the Reynolds stresses.

For a multigrid correction, a similar limitation as for the coarse grid correction of the turbulence quantities is used. Details can be found in Paper 2.

3.4 Limitations of the Reynolds stresses

Reynolds stresses cannot get arbitrary values, since there are some physical limitations that Reynolds stresses must obey (Paper 5). These are generally called realizability conditions [32]. There are two such conditions: the diagonal components of the Reynolds stresses must be equal or greater than zero

$$\overline{\rho u_i'' u_j''} \geq 0 \quad \text{if } i = j; \quad (3.27)$$

and the absolute value of the off-diagonal components must be smaller than the square root of the multiplication of corresponding diagonal terms

$$\overline{\rho u_i'' u_j''} \overline{\rho u_i'' u_i''} \leq \overline{\rho u_i'' u_i''} \overline{\rho u_j'' u_j''}. \quad (3.28)$$

Proof for the first condition is trivial. Proof for the second condition can be found in [30].

Source terms in turbulence equations should be such that these limits will never be violated. The RSM used does not fulfil the above conditions in some extreme academic cases. However, anyone who has performed calculations with higher-order methods knows that there might be overshoots during the iteration, or even in the final results. This will occur even if the turbulence model is realizable. Because of these, limitations, Eqs. (3.27) and (3.28) are checked after every iteration sweep explicitly. It was found that when the limitations are active, especially for the off-diagonal terms, the stability increases.

3.5 Parallel Computing

For over a decade, parallelization has been used to enhance the efficiency of flow solvers. The basic idea is to divide the computing work between many simultan-

ously running processors. The challenge is to design algorithms so that all processors have a full load all the time. This requires that the work load of the processors is equal and also the amount of communication between the processors is small and fast. Details of the original parallelization are given in Paper 3. Here, a summary is presented with some recent progress and results.

The simplest method of parallelization that can be used with shared-memory machines takes place on the DO-loop level. This can be done automatically by an advanced compiler. However, it is effective only with a very limited number of processors and is limited to shared-memory machines. Better performance from a large number of processors can be obtained by dividing the space into smaller sub-domains. A common approach applied, e.g. in [33, 34], is to divide the computational domain into equally sized blocks and to apply message passing between the blocks.

During this work the parallelization has been based on the Message Passing Interface (MPI) standard [35]. The computational domain is divided into blocks and the block boundaries are updated using MPI. In order to get a balance between the processes, the blocks should be of an equal size. However, the code can handle several (smaller) blocks in one process. This property can be utilized especially with small tasks and with a small number of processors, when a good load balance is not so critical.

Parallelization using MPI

A common parallelization tool, the Message Passing Interface (MPI) standard [35] has been used to keep the code as portable as possible. The computational cycle is described in Fig. 3.1. One processing element (PE0) is the master and others are slaves. The updating of boundaries between different processes is most important if the performance is of concern. Due to the development history of the code, the communication between the boundaries was performed for each variable to be solved separately in earlier work in Paper 4. In the most recent developments, a boundary value data is packed up in one vector that is sent to neighboring processors [36]. Large vectors of data are more efficient than a large number of smaller ones. The order of connection is determined at the beginning of the computing so that most of the processors can communicate simultaneously and no dead-lock situation is possible.

Parallel Performance

The parallelization can be tested using two different approaches. One is to keep the size of one process computation work constant, i.e. scaling. This means that the total problem size increases as the number of processes increases. For example, if a problem size is 32^3 for one processor then the size of a two-processor run will be twice the 32^3 grid (e.g. $64 \times 32 \times 32$ grid). Another approach is to keep the total problem size constant and divide it between the processes. In the following this is called blocking. If the problem size is 32^3 for one processor, then a two-processor

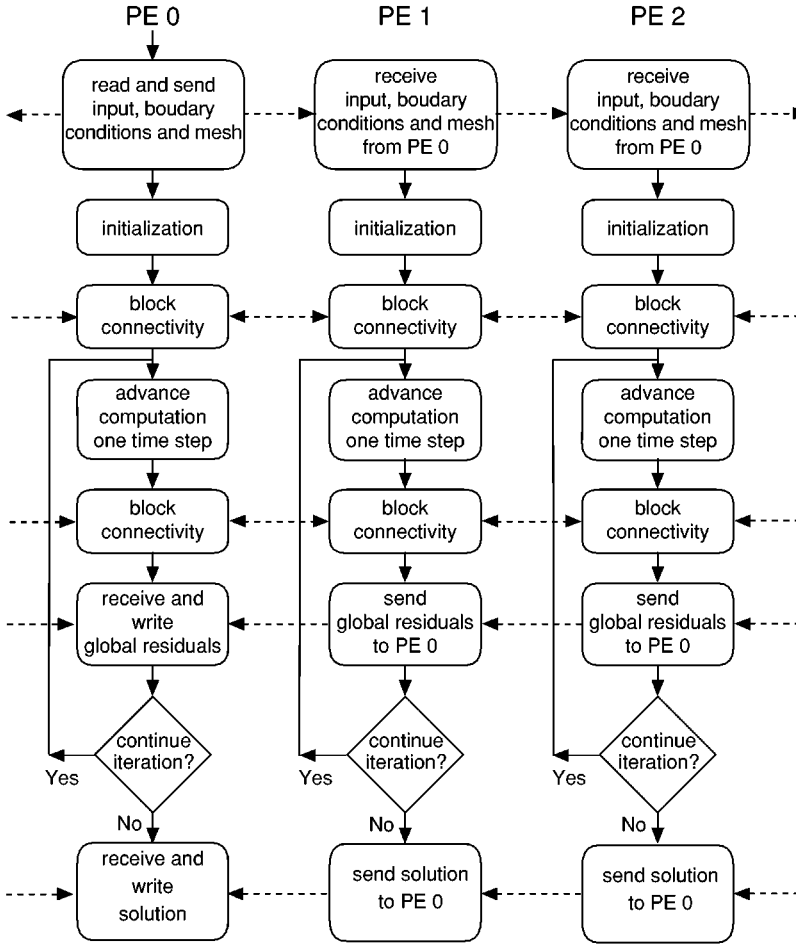


Fig. 3.1: A flow diagram of the parallelized code. Communication between the processors is depicted by horizontal dashed lines.

run will be of the same size but one processor work will be only half of the original size (e.g. $32 \times 32 \times 16$ grid).

Performance tests were carried out with two different types of computers. One was a massively parallel processing (MPP) Cray T3E computer with a maximum 224 of processors (only 64 were used in this study), and the other was a cluster of personal computers. The performance results shown for the T3E computations are from Paper 3 and for the PC cluster from Ref. [36, 37]. The PC cluster contains 16 Dell precision workstation 410 computers. Each computer has Dual Intel Pentium II 400 MHz processors with 128 Mbytes of memory. The computers are connected to each other by a 100 Mbit Ethernet. The operating system is Linux.

In order to test the performance of the scaling, the flow past a cropped delta wing was calculated at $Ma_\infty = 0.85$, $Re_\infty = 4.5 \times 10^6$ and $\alpha = 0^\circ$ or $\alpha = 10.76^\circ$. Grids

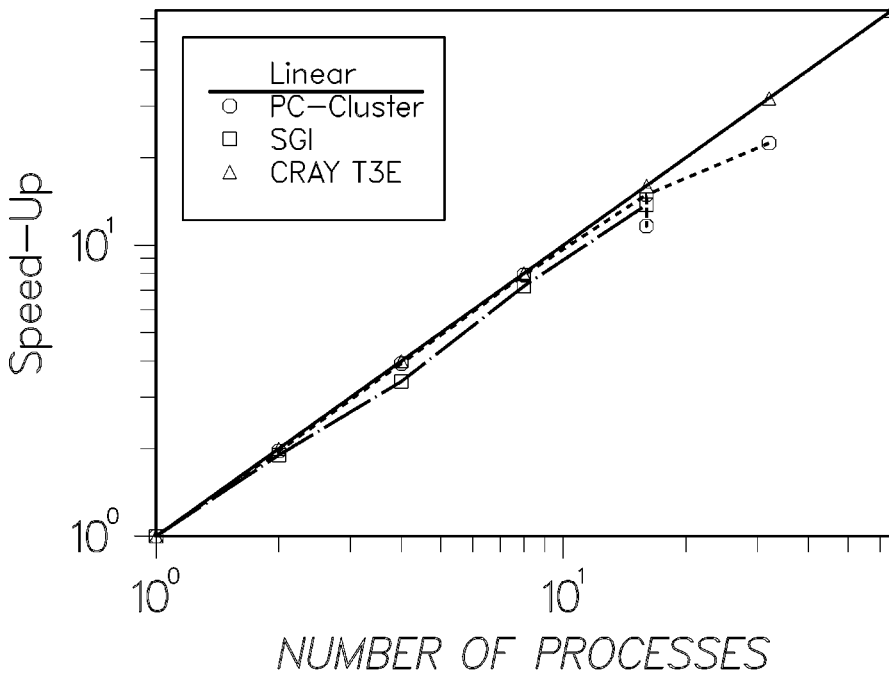


Fig. 3.2: Speed-up of the parallelization in scaling.

were generated so that all the blocks had a size of $32 \times 32 \times 32$. The computational domain size was from one to 64 different blocks, and each block was calculated in a different process. On the PC cluster, the largest case contained 32 blocks. Thus the coarsest grid had 32 768 and the densest grid 1 048 576 computational cells on the PC cluster.

The speed-up was determined directly from the absolute time spent in the calculation. The results are presented in Fig. 3.2. It can be seen that a perfect scaling is achieved in these test runs with the T3E up to 64 processes. The PC cluster had a good scaling up to 16 processors. It can be estimated that the code is parallelized in this way so well that it could be run with over a thousand processors in MPP systems.

The efficiency of the parallelization was also tested in a case of blocking. With the T3E the grid size was $64 \times 64 \times 32 = 131\,072$, and for the PC cluster the grid size was $192 \times 80 \times 40 = 614\,400$. In both cases the size was limited by the processor memory size in the T3E and in the PC cluster. Because of the different block sizes, the comparison is not straightforward. The partly unexpected results are shown in Fig. 3.3. Firstly, the performance curve is somewhat better for the PC cluster than for the T3E. The situation is different for the PC cluster because the block sizes are larger in the PC cluster than in the T3E simulation. Secondly, the parallelization is better for the PC cluster for blocking than for scaling. One explanation can be that the single-processor performance increases when the size of the problem in one

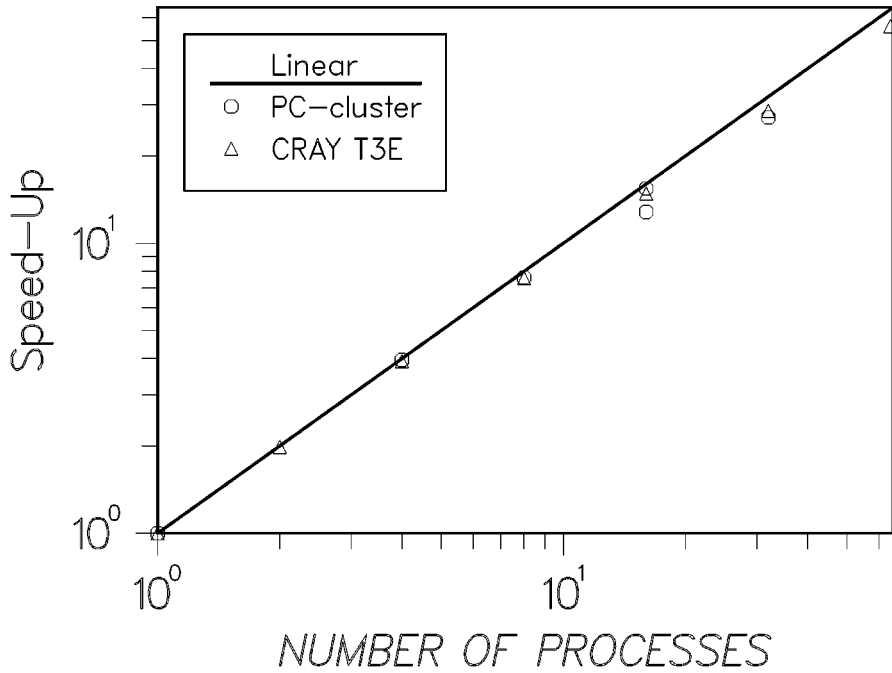


Fig. 3.3: Speed-up of the parallelization in blocking.

processor is decreased. This phenomenon is called super-linear scaling. It seems that the PC cluster is more sensitive to the problem size, and on the other hand also the block size used in T3E is not sufficiently large.

It can be concluded that the performance of the flow solver has been increased by two order of magnitude during this work. This was done by using parallelization. Parallel implementation is based on the MPI standard, and thus, it is platform independent. With optimal cases, the parallelization is excellent. However, in reality the computational domain cannot be divided in an optimal way. An example of a non-optimal case is presented in the following chapter.

4 Validations

The turbulence models used have been validated with various flow problems. These vary from a simple channel (Paper 1) to a centrifugal compressor (Paper 5) or nuclear reactor thermal hydraulics (Paper 6). A part of the validation has been made in the annual ERCOFTAC/IAHR workshops on refined turbulence modelling. Most of these test cases were not published separately by the author but can be found in the proceedings of the workshops. Altogether, the methods are validated with ten problems in this work. Table 4.1 shows a summary of the test cases.

In most of the flows the Reynolds-stress model (RS), the explicit algebraic Reynolds-stress model by Gatski *et al.* (GS) and Chien's $k - \varepsilon$ model (CH) were used. In the following, all the problems are briefly described and some of the results are shown.

4.1 Channel Flow

The Reynolds-stress model was implemented and tuned using a simple channel flow. In addition the damping function that switches from Shima's model to the SSG model was designed originally for the channel flow. The channel flow was chosen for simplicity and the well-defined DNS data by Kim *et al.* [3]. The results are given in Papers 1 and 2 for Shima's model. The effect of the damping function

Table 4.1: Summary of the test cases.

Case	Reference	ERCOFTAC WS
Channel flow	Papers 1 and 2	
Rotating channel flow		7th
Boundary layer flow	Paper 7	
Wall jet		5th and 6th
Curved duct	Paper 2	5th
Surface-mounted cube		6th
Matrix of surface-mounted cubes		8th
Return channel	Paper 4	
Centrifugal compressor	Paper 5	
Turbulent Mixing in Core of Nuclear	Paper 6	
Reactor Fuel Bundle		

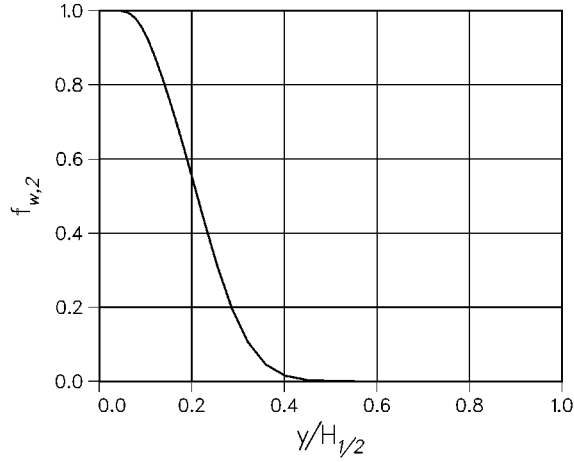


Fig. 4.1: Effect of the damping function in the channel. If $f_{w,2} = 1$, Shima's model is applied and if $f_{w,2} = 0$ the SSG model is applied for the pressure-strain term.

$f_{w,2}$ Eq. (2.58) is shown in Fig. 4.1. In this case the $y^+ = 180$ at the centre of the channel. This means that the SSG pressure-strain model is applied as $y^+ > 70$.

4.2 Rotating Channel

This test case was presented at the 7th ERCOFTAC workshop on refined flow modelling [38]. The considered flow is fully developed in a channel rotating in an orthogonal mode. The flow is at a low-Reynolds number and DNS data is available for a range of rotating rates. The Reynolds number, based on the bulk velocity and the channel half-width is around 2 900. The rotation number $Ro = 2\Omega h/U_b$ varies from zero to 0.5.

This problem is rather simple and thus, some exotic turbulence models could be used. The flow is semi two-dimensional. This means that the flow equations are reduced to one momentum and one continuity equation. The computations are performed using an implicit time-marching computer code FULFLO [39].

Four different turbulence models are tested:

1. Wilcox's standard $k - \omega$ model [13,40] with a rotational correction, described below, applied in the ω -equation sink term [41].
2. Chien's low-Reynolds number $k - \varepsilon$ model [16] with the rotational correction applied in the ε -equation sink term.
3. EARSIM of Gatski *et al.* [14] with Wilcox's standard ω -equation and with the rotational correction applied in the ω -equation sink term.
4. RSM of Speziale *et al.* [18] with Wilcox's low-Reynolds number ω -equation.

Low-Reynolds number effects in the RSM are modelled by an elliptic relaxation method similar to Durbin [42].

Chien's $k - \varepsilon$ and Wilcox's $k - \omega$ models, excluding the rotational correction, are applied as in the original papers. Rotational correction is based on a generalized Richardson number [41]. Although the EARSM is sensitive to the rotation, it was found this kind of correction is necessary in order to get a correct velocity distribution.

Elliptic relaxation

The elliptic relaxation method is only used in this case, and thus, the methods are presented here. Following the work of Durbin [42], a relaxed pressure-strain tensor (\mathcal{P}_{ij}) which includes the conventional pressure-strain interaction and deviation of the dissipation-rate tensor from Rotta's dissipation model can be written as

$$\mathcal{P}_{ij} = \Phi_{ij} - \varepsilon_{ij} + \frac{\overline{u'_i u'_j}}{k} \varepsilon \quad (4.1)$$

This is solved from an elliptic relaxation equation

$$L^2 \nabla^2 f_{ij} - f_{ij} = -\frac{\mathcal{P}_{ij}^h}{k} \quad (4.2)$$

where $f_{ij} = \frac{\mathcal{P}_{ij}}{k}$ and \mathcal{P}_{ij}^h denotes a quasi-homogeneous form of \mathcal{P}_{ij} . In this work, more detailed functions are adopted from Pettersson *et al.* [43]. The right-hand side of Eq. (4.2) becomes

$$\frac{\mathcal{P}_{ij}^h}{k} = \frac{\Phi_{ij}^h}{k} + \frac{1 - \frac{1}{2}C_1}{T} 2b_{ij} \quad (4.3)$$

where Φ_{ij}^h is calculated by using the SSG model. Various functions are defined as

$$\begin{aligned} C_1 &= 2 + \frac{31}{8} A_2 \sqrt{A} & A_2 &= 4b_{ij}b_{ij} \\ A_3 &= 8b_{ik}b_{kj}b_{ji} & A &= [1 - 9(A_2 - A_3)/8] \\ b_{ij} &= \frac{\overline{u'_i u'_j}}{2k} - \frac{1}{3}\delta_{ij} & L &= \tilde{C}_L \sqrt{\frac{k^3}{\varepsilon^2}} + \tilde{C}_\eta \sqrt{\frac{\nu^3}{\varepsilon}} \\ \tilde{C}_L &= C_L A_2^{1/2} & \tilde{C}_\eta &= C_\eta A_2^{-1/2} \exp \left[- \left(\frac{1 + A_3}{0.1 + A_2} \right)^2 \right] \\ T &= \sqrt{\left(\frac{k}{\varepsilon} \right)^2 + C_T^2 \frac{\nu}{\varepsilon}} \end{aligned} \quad (4.4)$$

and the coefficients are

$$\begin{aligned} C_L &= 0.25 & C_\eta &= 647 \\ C_T &= 6 & C_K &= 0.22 \end{aligned} \quad (4.5)$$

Pettersson used a value of 0.18 for C_L but this did not give satisfactory results in this study.

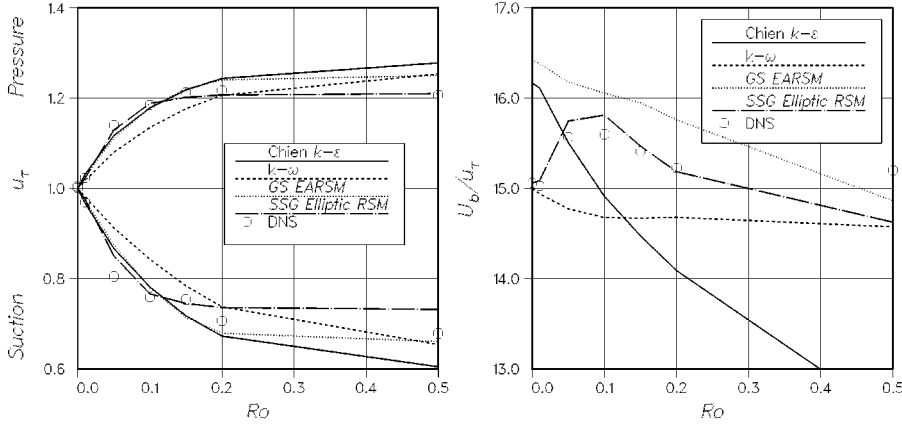


Fig. 4.2: Friction velocities for both walls of the channel and the averaged friction.

Boundary conditions for the elliptic relaxation

The boundary conditions for the elliptic relaxation are modified from Durbin and Pettersson's approaches. In general, boundary conditions can be written as

$$\begin{aligned} f_{22} &= -\frac{20\nu}{\varepsilon_{wall}} \left(\frac{\overline{u'_2 u'_2}}{y^4} \right)_1 & f_{12} &= -\frac{20\nu}{\varepsilon_{wall}} \left(\frac{\overline{u'_1 u'_2}}{y^4} \right)_1 \\ f_{11} &= 0 & f_{33} &= -f_{22} \end{aligned} \quad (4.6)$$

Since, no difference can be made between the streamwise and the spanwise directions in more complicated flow simulations, the boundary conditions for f_{11} and f_{33} are rewritten as

$$f_{11} = -\frac{1}{2}f_{22} \quad f_{33} = -\frac{1}{2}f_{22} \quad (4.7)$$

The value of $\left(\frac{\overline{u'_i u'_j}}{y^4} \right)_1$ is not taken from the first computational cell adjacent to the wall, instead it is integrated from the wall with a proper length scale. In this way, the elliptic relaxation method becomes fairly grid independent, it is not sensitive to the height of the first cell and it is numerically stabilized. In this way the boundary conditions do not need to be taken into account implicitly.

Results

The resulting wall-friction velocities are seen in Fig. 4.2. It can be seen that all the models predict quite a good asymmetry in the friction shown on both walls, whereas the averaged friction on the right-hand side of the figure is superiorly predicted by the RSM.

It was found within this study that the EARSM is sensitive to the rotational effect but this effect is too weak. The RSM was the only one that could predict the shape of the averaged friction as a function of the rotation number. The elliptic relaxation method gives promising results, but the method is complex and difficult to

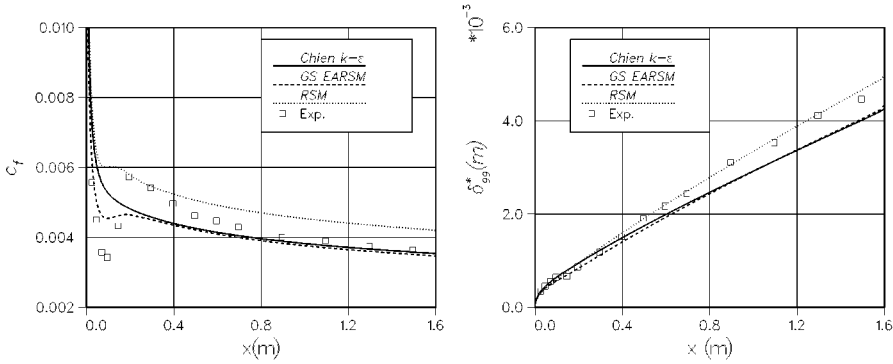


Fig. 4.3: Skin-friction coefficient and the displacement thickness.

apply in 3-D simulations because of the boundary conditions. It is not straightforward to apply boundary conditions for arbitrary curvilinear solid boundary surfaces. Questions arise as to how the function f_{ij} should be rotated and in the 3-D flows there are also two additional Reynolds stresses and thus boundary conditions for appropriate f_{ij} should be redesigned.

4.3 Flat-Plate Boundary Layer

The third problem is a flat-plate boundary layer with a high free-stream turbulent intensity. The problem was taken from the ERCOFTAC Fluid Dynamics Database WWW Services maintained by Dr. Voke. Experimental results for this flow have been provided by John Coupland (Rolls-Royce). In this simulation the flow was simulated up to $Re = u_\infty L_x / \nu \approx 10^6$. More details of the boundary conditions and the computational grid can be found in the reference by the author [44] and also in Paper 7.

This simulation indicated that the skin-friction coefficient is overestimated with the Reynolds-stress model. Because of this simulation, the constant γ in Eq. (2.57) was modified to $\gamma = 0.055$. Figure 4.3 shows the skin friction and the displacement thickness for the turbulence models that were used. No transition model is applied. However, in this simulation the GS and RS models predict weak transition-like skin-friction distributions. Further downstream, the CH and GS models predict the skin-friction coefficient correctly, whereas the RS model overpredicts it even after modifications in parameter γ .

4.4 Wall Jet

The next test case is a two-dimensional plane wall jet that enters along the bottom of a large pool, through a thin slot. The results were compared against LDA measurements available [45]. The plane wall jet was a test case in the 5th and the 6th

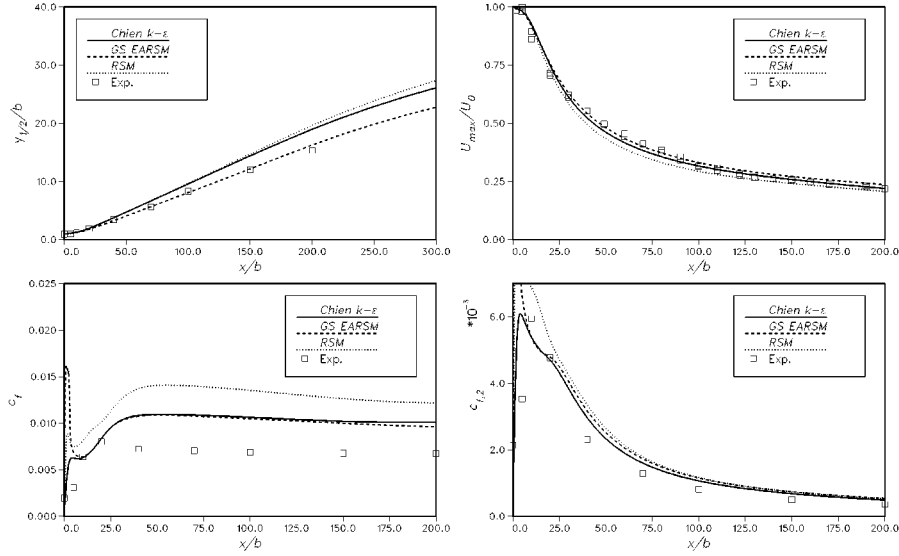


Fig. 4.4: Spreading rate, maximum velocity decay and two friction coefficients for jet flow problem.

workshops. It is featured as a boundary layer flow as well as a jet flow.

The flow enters in from a 1 cm-wide slot. The dimensions of the pool are $7.45 \text{ m} \times 1.35 \text{ m}$. The inlet velocity is 1 m/s, which corresponds to the inlet Reynolds number $Re = U_0 b / \nu = 10\,000$ (here b is the slot height of the jet). The kinematic viscosity of water at 18°C is $\nu = 1.05 \times 10^{-6} \text{ m}^2/\text{s}$. At the inlet, only the u -velocity and u' -fluctuation component were measured and could be directly utilized as boundary conditions. Since w' and v' are unknown at the inlet, their mutual contribution to the turbulence kinetic energy k is approximated to be equal to the contribution of u' alone. Thus, k is approximated as $0.65u'u'$ ($v' = 0$ and $w' \approx 0.3u'$).

An orthogonal grid is used to simulate the whole pool. The grid consists of 64 cells in the direction of the jet (i) and 80 cells in the jet normal direction (j). The grid is heavily clustered in the j -direction to the pool bottom wall and 32 cells are placed inside the inlet slot height. There is also clustering in the i -direction so that the majority of the cells in the i -direction lies inside the area of interest. Near-wall cells in the j -direction extend to a distance of about $3 \times 10^{-5} \text{ m}$ ($y_{max}^+ = 1.6$), and in the i -direction they extend to a distance of about $1.1 \times 10^{-3} \text{ m}$. Surface of the pool is considered as a mirror boundary condition.

Figure 4.4 shows the main parameters of the jet flow. In the figure, $y_{1/2}$ is a distance from the wall to the points where the jet velocity is half of the local maximum velocity U_{max} . The friction coefficient c_f is made dimensionless with the local maximum velocity and $c_{f,2}$ with the inlet velocity U_0 . It can be seen that the spreading rate is best predicted by the GS model. The RSM overpredicts the skin-friction coefficient here as well as in the boundary layer case. A decay of the maximum velocity is largest with the RSM, and that is why the skin-friction

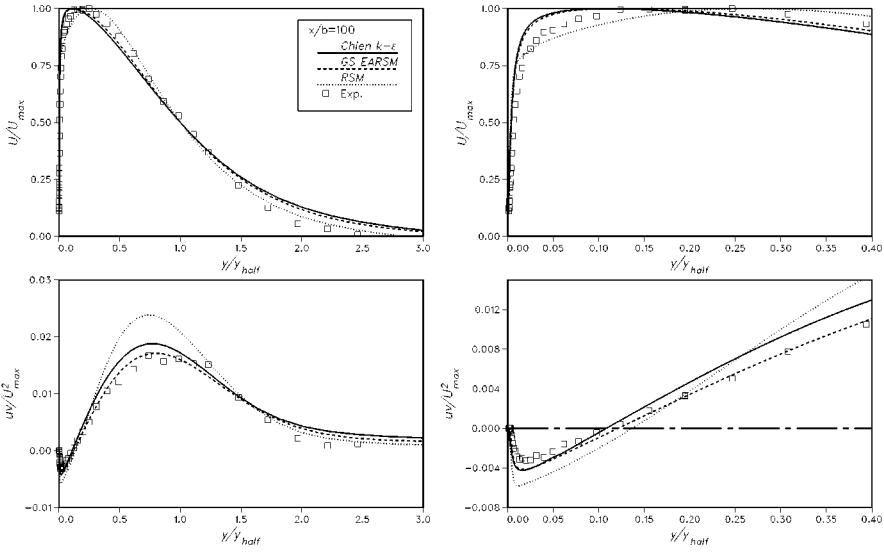


Fig. 4.5: Non-dimensional velocity and shear-stress distributions at station $x/b = 100$. The right-hand side is a closer view next to the solid surface.

coefficient c_f is not particularly well captured.

Figure 4.5 depicts the local velocity and turbulent shear-stress magnitudes. In this station, at a distance of $x/b = 100$ from the nozzle, the jet is in a self-similar state. The variables are made non-dimensional by the jet-stream half-width $y_{1/2}$ and the local maximum velocity U_{\max} . The two-equation models, both the linear and the nonlinear alternatives, give coincidental locations of zero shear stress ($\overline{u''v''} = 0$) and zero mean velocity gradient ($\partial U / \partial y = 0$). This well-known deficiency of the two-equation models (CH and GS) can be clearly seen in the right-hand side of the figure. The velocity profile at the outer region is better predicted by the RSM, whereas the shear-stress magnitude is overpredicted by the RSM, which partly explains the largest decay of the maximum velocity in Fig. 4.4.

4.5 Curved Duct

As a first three-dimensional problem, a flow in a curved duct [46] is considered. This problem was presented in the 5th ERCOFTAC workshop on refined turbulence modelling [47] and in Paper 2. The duct, shown in Fig. 4.6, has two straight parts and a curved section. The rectangular cross-section of the channel has a width of $H = 20.3$ cm and a height of $6 \times H$, as seen in the figure. Only half of the channel is simulated. The Reynolds number based on the free-stream velocity and the channel width H is 224 000. This problem is featured by two types of secondary vortices: a turbulent driven vortex before the bend, and a pressure driven vortex at and after the bend. The simulation was performed with a grid size of $64 \times 48 \times 128$. The inlet boundary conditions are taken from the experiments. This simulation was the

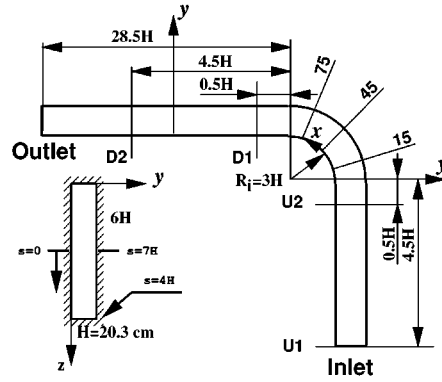


Fig. 4.6: Geometry and measurement stations of the curved duct.

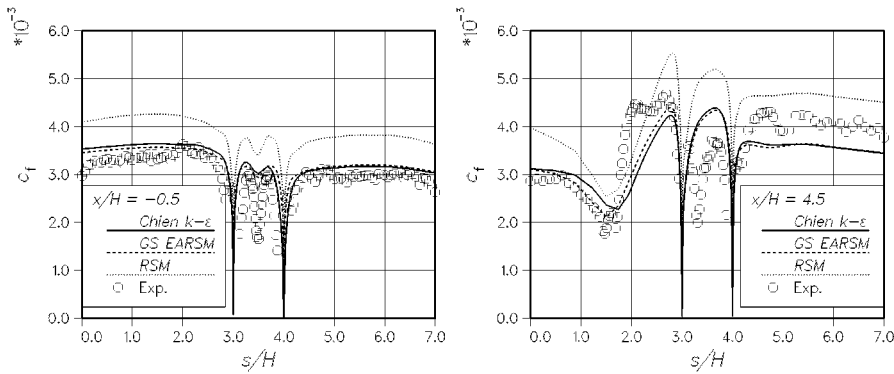


Fig. 4.7: Friction coefficient along the channel wall at stations U2 and D2.

first parallel computing task accomplished in this work. The computation was done with four processors.

The friction coefficient is presented in Fig. 4.7 at station $U2$ ($x = -0.5H$), before the curve, and at station $D2$ ($x = 4.5H$), after the curve. Coordinate s is defined in Fig. 4.6. As can be seen, the friction is again overestimated with the RSM. On the right-hand side of Fig. 4.7, at station $D2$, the experiment indicates an existence of Görtler-type vortices (scattering in skin friction within a distance of $5 < s/H < 7$) where none of the models shows any indication of it. It is also possible that the grid might be too coarse in that region to capture the vortices. If the friction is studied the CH and GS models perform better than the RSM. Although not shown here, the velocity distributions show similar accuracy for all the models.

4.6 Surface-Mounted Cube

A surface-mounted cube was one of the test cases in the 6th ERCOFTAC turbulence workshop. This case was taken in the workshop in order to make a comparison

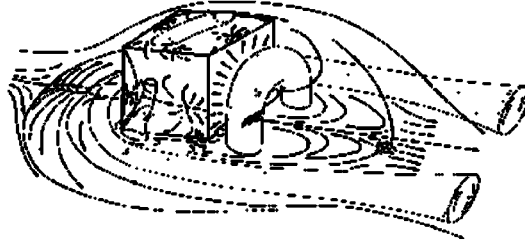


Fig. 4.8: Schematic figure of the flow around a surface-mounted cube [49].

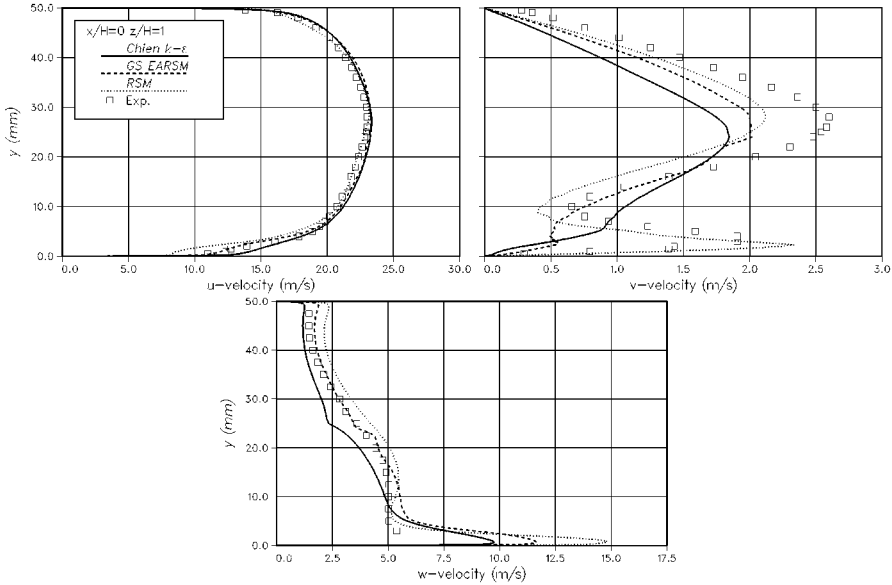


Fig. 4.9: Velocities at a side of the cube, u -component is streamwise direction, v perpendicular to the channel wall and w is spanwise direction.

between the RANS simulations and LES. It was also used in the ERCOFTAC LES workshop [48].

The flow around a single cube with a side of $H = 25$ mm placed on the bottom wall of a plane channel was measured by Martinuzzi *et al.* [49] with the LDA technique. A channel height was $h = 50$ mm and the corresponding Reynolds number $Re_h = 8 \times 10^4$. A schematic figure of the flow is shown in Fig. 4.8.

The computation was made with the CH, GS and RS models. The grid consists of four blocks and the total number of cells is 884 736. Computing was done using 19 parallel nodes of the Cray T3E computer.

The RANS models give good results at the frontal stations of the cube but behind the cube the results are not satisfactory. The steady-state RANS calculations do not capture the mixing of the vortex shedding behind the cube. A time-accurate LES captures the flow much better behind the cube [48]. The velocity profiles at two different stations are shown in Figs. 4.9 and 4.10. The first station is at the

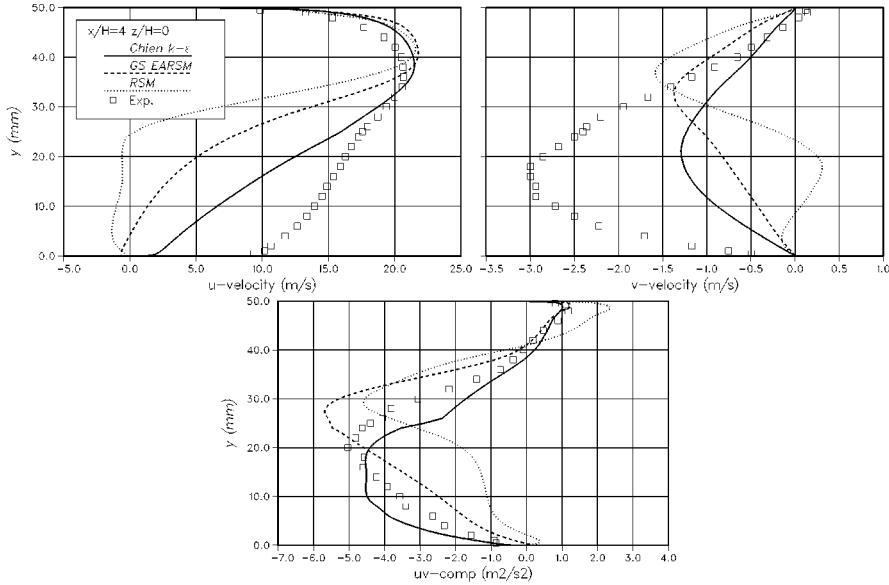


Fig. 4.10: Velocities at the distance of three cube heights downstream from the cube, u -component is streamwise direction, v perpendicular to the channel wall and uv is Reynolds-stress component.

side of the cube where the RANS models work well, and the second one is at the wake where the RANS results are poor. At the side of the cube all models predict quite a good u -velocity distribution. In the other directions, the Reynolds-stress model predicts a better agreement with the experimental data. At the station behind the cube, the re-circulation zone is overestimated by all the models. As mentioned above, the steady-state RANS does not seem to capture the vortex shedding. Behind the cube the CH model gives the best results.

4.7 Matrix of Surface-Mounted Cubes

This problem is closely related to the previous one. However, the boundary conditions can be easily defined because the periodicity can be utilized. This problem was used in the 6th, 7th and 8th ERCOFTAC turbulence-modelling workshops. The results of the most recent workshop can be seen in the proceedings edited by the present author [50].

A matrix of cubes, ($H = 15$ mm) is placed on the bottom wall of a two-dimensional channel with a height of $h = 51$ mm. The space between the cubes is $3H$. The bulk velocity is $u_b = 3.86$ m/s and the corresponding $Re_h = 1.3 \times 10^4$. A sketch of the geometry is shown in Fig. 4.11. A two-component back-scatter LDA system was used to measure the velocity components [51].

The computation was made with the CH, GS, RS models and a variant of the $k - \omega$ model [41, 52]. The computational grid consists of 635 904 control volumes in nine blocks. Because the flow is virtually fully developed, the periodic boundary

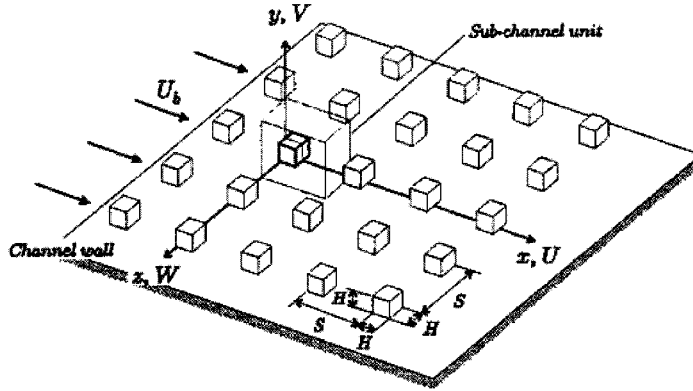


Fig. 4.11: View and coordinate system of the cube matrix in a channel [51].

conditions could be used.

Figure 4.12 shows the u -component of the velocity, $\widetilde{u''u''}$ - and $\widetilde{w''w''}$ -profiles. The profiles are drawn in a vertical plane ($z/H = 0$). It can be seen that the RSM predicts the velocity profile better close to the bottom wall, but right next to the wall, the RSM does not capture the rise of the back flow velocity. The $k - \omega$ model predicts too strong a reverse flow. However, at the upper part of the channel, the $k - \omega$ velocity profile is in good agreement with the experimental data. The profiles of the u - and w -velocity components, and the $\widetilde{u''w''}$ -shear-stress are drawn in a horizontal plane ($y/H = 0.5$) in Fig. 4.13. In this direction none of the models predict the cross-flow component w to be strong enough. It was found in the 8th ERCOFTAC turbulence-modelling workshop [50] that LES or DNS captures velocity profiles better than the RANS simulations also in this case. On the basis of this example it is assumed that the steady-state RANS cannot capture-vortex-shedding type phenomena accurately. The full Reynolds-stress model predicts the cross-flow somewhat better than the eddy-viscosity assumptions, whereas in this case the GS model does not seem to give any improvement.

The comparison of the Reynolds-stress profiles for the linear two-equation models is somewhat fuzzy because the eddy-viscosity assumption works well for the off-diagonal component, but not well for the diagonal components. Therefore, it is slightly surprising that Chien's $k - \varepsilon$ model predicts the best profiles for the Reynolds stresses in Fig. 4.12. However, the shear-stress component $\widetilde{u''w''}$ is best captured by the RSM in Fig. 4.13.

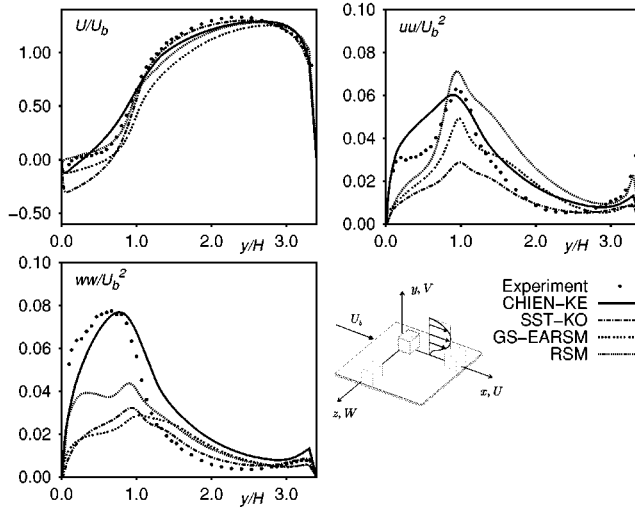


Fig. 4.12: Profiles in the y -direction for the u -velocity component, $\widetilde{u''u''}$ and $\widetilde{w''w''}$ are drawn in a vertical plane ($z/H = 0$), located 1.3 cube lengths downstream from the cube ($x/H = 2.3$).

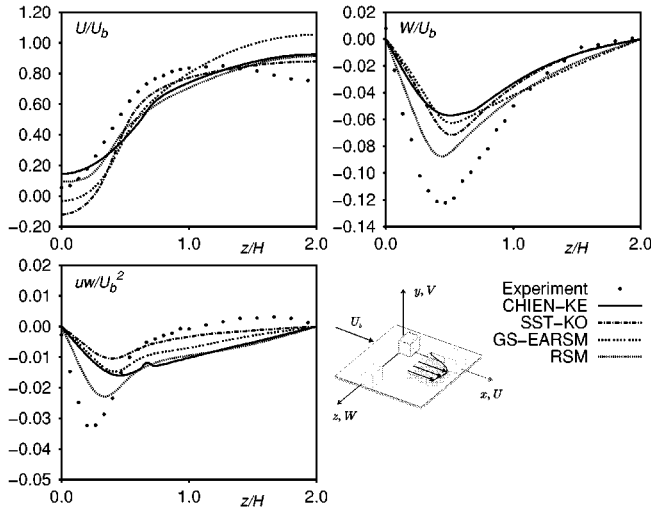


Fig. 4.13: Profiles in the y -direction for the u - and w -velocity components, and $\widetilde{u''w''}$ -shear-stress component are drawn in a horizontal plane ($y/H = 0.5$), located 1.3 cube lengths downstream from the cube ($x/H = 2.3$).

4.8 Return Channel

The next test case is a flow in a return channel. The geometry of the present test case given in Fig. 4.14 is typically used to join the exit from the first stage of a centrifugal machine to the inlet of the second stage. Experiments are provided by Concepts ETI, Inc. [53]. A flow field in the return channel is affected by a

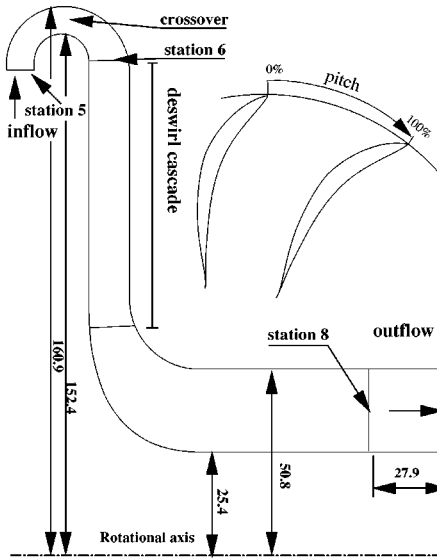


Fig. 4.14: Geometry of the return channel.

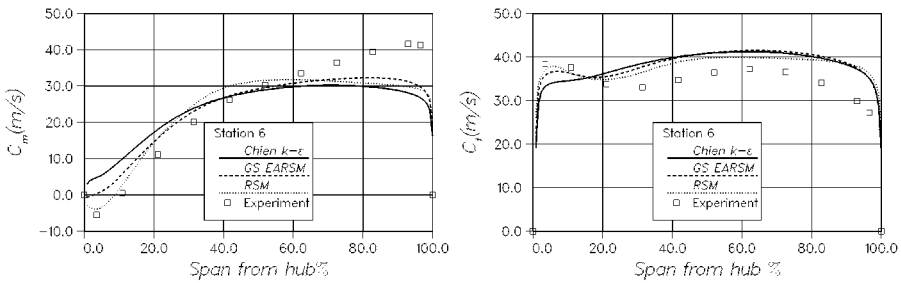


Fig. 4.15: Pitch-averaged meridional velocity C_m and tangential velocity C_t from the hub to the shroud at station 6.

strong streamline curvature, separations take place and three-dimensional vortices occur. Hence, simulation of this flow is a highly demanding test for turbulence modelling. Because of the asymmetric stretching of the velocity field, it is expected that Reynolds-stress models perform better than a traditional two-equation model. This simulation is presented in Paper 4.

The CH, GS and RS models were applied for this problem. Only one deswirl channel is simulated and the grid size is 655 360. The computational domain begins at station 5 (see Fig. 4.14). Experimental values are set for the velocities corresponding to the average inlet Mach number 0.15.

Measurement station 6 is located after the crossover at the leading edge of the deswirl cascade. The profiles for the meridional and tangential velocities are shown in Fig. 4.15. Station 8 is located 47.8 mm after the bend (see Fig. 4.14) and the velocity profiles are shown in Fig. 4.16. The RS and GS models seem to predict

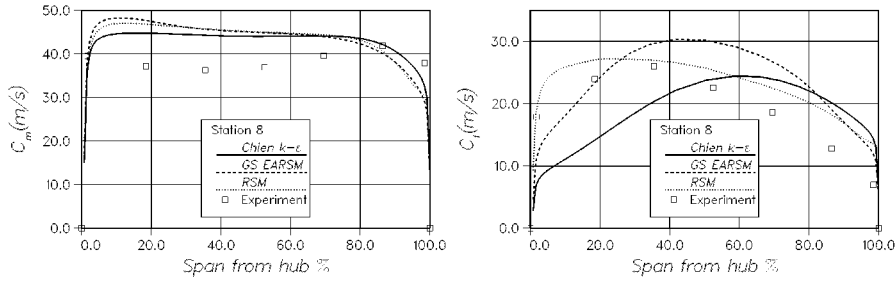


Fig. 4.16: Same as in Fig. 4.15 at station 8.

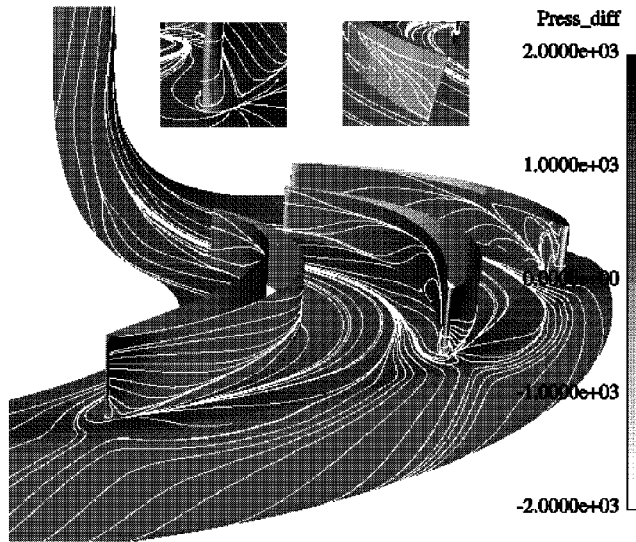


Fig. 4.17: Surface streamlines at the deswirl cascade and at the bends with the GS model. The inset figures are from the leading and trailing edge regions.

the flow better than the simpler CH model. For example, the tangential velocity at station 6 contains a peak close to the hub, which is captured well by the RSM. The GS model also predicts the peak, but it is smaller. All the turbulence models have difficulties at the shroud area. They underpredict the meridional velocities and overpredict the tangential velocities. At the hub region of station 6, the size of the separation bubble can be estimated from the meridional velocities in Fig. 4.15. The RSM predicts the strength and the size of the bubble well. At station 8, the meridional velocities are predicted similarly for all the methods, but the shape of the tangential velocity is captured only by the RSM. Again, the GS model results are somewhat better than the CH model.

Surface streamlines are shown in the case of the GS model in Fig. 4.17. Complex three-dimensional separations and vortices are seen in the flow field. For example, at the leading edge of the vane, separation occurs on the pressure side. Separation takes place also at the trailing edge.

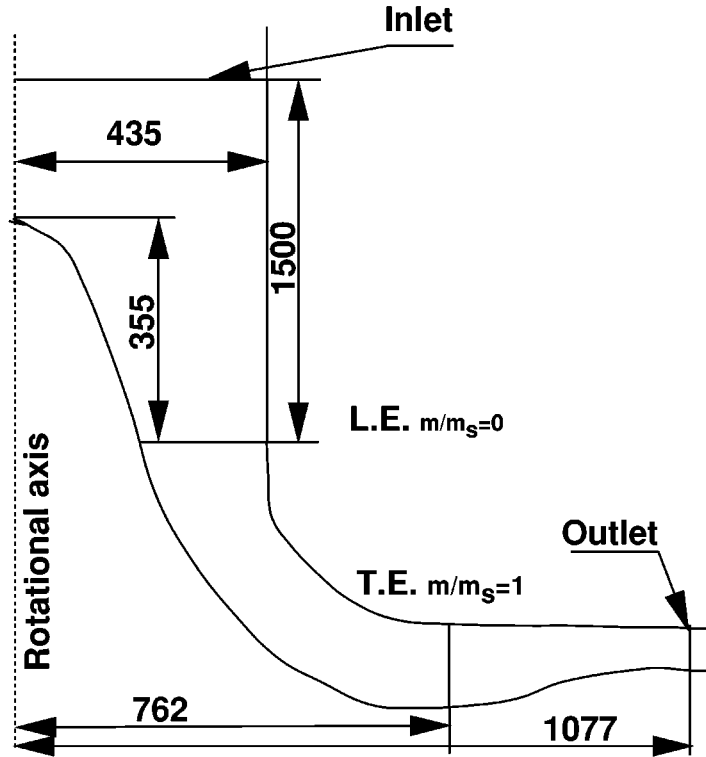


Fig. 4.18: Geometry of the low-speed compressor. The units are in millimetres.

4.9 Centrifugal Compressor

The NASA low-speed compressor is the next test case [54]. In this study the GS model was not applied, but instead the algebraic Baldwin-Lomax (BL) model [9] was used. The simulations and details of the BL model are described in Paper 5.

The test case is a backswept impeller with a design tip speed of 153 m/s. The main dimensions can be seen in Fig. 4.18. The impeller is followed by a vaneless diffuser that generates axisymmetric outflow boundary conditions. The impeller has 20 blades with a backsweep of 55° . The inlet radius is 0.435 m and the exit radius 0.765 m. The clearance between the impeller blade tip and the shroud is a constant 2.54 mm from the impeller inlet to the impeller exit. This is also modelled in the simulation. The mass flow rate is 30 kg/s and the rotation speed 1862 rpm at the design point. With these values the total pressure ratio over the impeller is roughly 1.14, the temperature ratio 1.04 and the adiabatic efficiency 92.2 per cent.

Extensive experimental results are provided by Hathaway *et al.* [54]. The experimental data contains velocity measurements from 20 survey planes, pressure distributions on the blade surfaces and on the shroud, performance measurements and some flow visualizations. In the simulation only one passage is modelled. The grid size is 1 281 024 computational cells and it contains five different blocks.

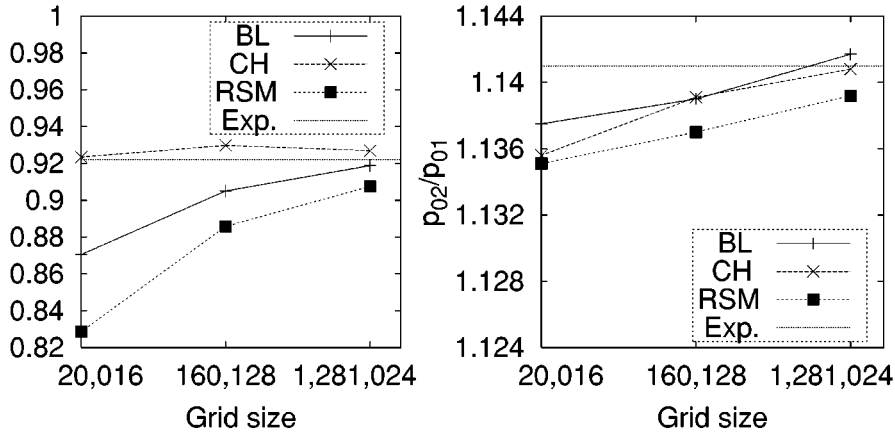


Fig. 4.19: Adiabatic efficiencies and total pressure ratio for different models and grid sizes. The left-hand side is the efficiency and the right-hand side is the total pressure ratio.

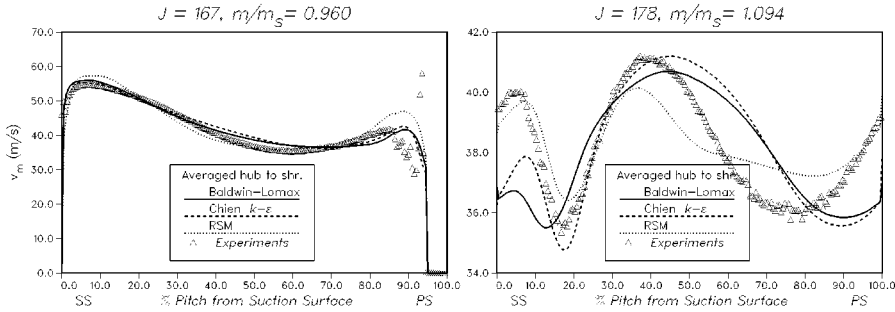


Fig. 4.20: Meridional velocities v_m from suction surface (SS) to the pressure surface (PS). Velocities are averaged from hub to shroud. The results are close to the trailing edge (left) and after the trailing edge of the impeller (right).

Figure 4.19 shows the efficiencies and pressure ratios across the impeller with different models and with different grid densities. It can be seen that the total to static efficiencies are very close to the experimental values for the BL and CH models. It should also be noted that the CH model predicts good values for a very coarse grid size with only 20 000 nodes. The RSM seems to predict a bit lower values for the efficiency. The BL and CH models predict exactly the correct value for the total pressure ratio with the densest grid, whereas the RSM predicts a somewhat lower value again. Lower efficiencies and pressure ratios for the RSM could be explained by the higher skin friction, as is generally predicted by the present RSM.

Figure 4.20 depicts the meridional velocities at 96 per-cent distance downstream from the leading edge and 9.4 per-cent downstream from the trailing edge. The velocities are averaged from the hub to the shroud. The velocity distributions are quite similar inside the impeller channel. After the impeller, the RSM seems to predict the history effect caused by the impeller blades better.

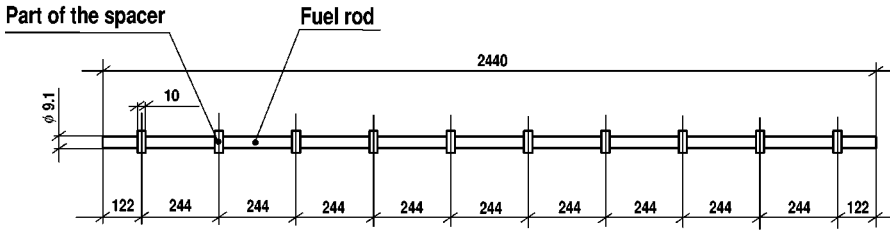


Fig. 4.21: Main dimensions of a fuel rod [mm]. The diagram is not to scale.

4.10 Turbulent Mixing in the Core of a Nuclear Reactor

As an example of the efficiency and the importance of parallel processing, the simulation of a fuel bundle of a nuclear power plant is described. More details of the thermodynamic behaviour of a fuel rod bundle can be found in Paper 6. The purpose of this study was to predict the turbulent mixing of the temperature inside a core.

The Loviisa VVER-440 units are of the pressurized water reactor-type (PWR), and thus, the cooling of the reactor core under normal operation is done by water that can reach a subcooled boiling state only locally. The fuel is located in the rods that are bound up as a bundle. Each bundle has 126 fuel rods. The dimensions of a single rod are shown in Fig. 4.21. The top of the bundle is shown in the Fig. 4.22. For the simulation only one twelfth of a fuel rod bundle is modelled. This 30° sector contains six full and nine half rods. The volume grid has 7 784 640 cells in 216 blocks. Turbulence is simulated with the CH model. The computations were done on a Cray T3E computer. As a main result of the simulations, the outflow fluid temperature distribution was predicted.

Because the simulations were run on a massively parallel computer, the Cray T3E, the computational domain had to be decomposed into sufficiently small blocks in order to obtain an acceptable balance between the processors (Paper 3). In this simulation, 128 of the total of 224 processors available were utilized. After the decomposition the grid consists of 303 computational blocks. The largest block contains 61 568 cells. In the original grid the largest block has 532 480 cells. Even if the grid is made up of simple H-type blocks, the topology is complicated owing to the large number of blocks. The boundary condition file contained 9 097 lines including 1 696 pairs of connections between the blocks. During an iteration cycle, the boundary conditions are updated in 2 554 patches by MPI. The number of variables changed in one patch is 13 000 on average, so altogether about 34 million variables are changed during each iteration cycle.

The simulation took roughly 5 days on the T3E with 128 processors. The efficiency of this parallelization was about 85 per cent. This means that if only one processor had been used, the simulation would have taken $5 \cdot 128 \cdot 0.85 = 544$

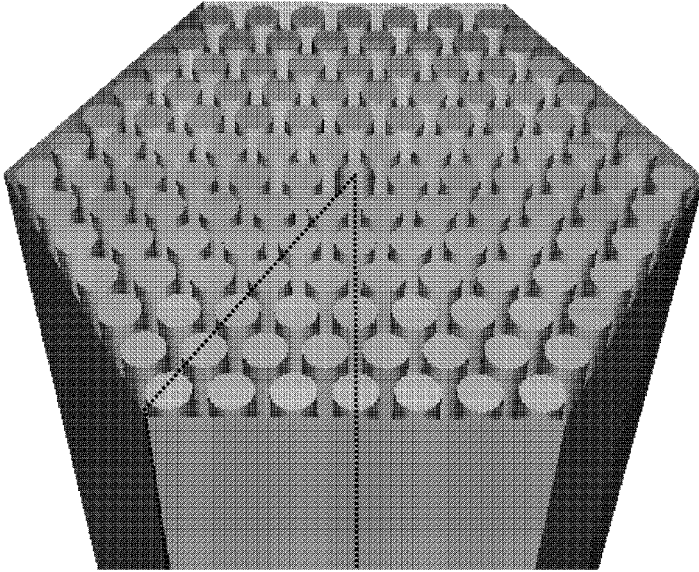


Fig. 4.22: Fuel rod bundle in its casing. One bundle contains 126 rods. The diameter of a fuel rod is 9.1 mm and the total length is 2440 mm. The simulation model can be seen as a dashed line.

days. The speed of the T3E processor is approximately one fourth of the speed of the latest workstation processors (SGI R12k), so the simulation would have taken roughly 140 days using only one R12k. This means that the simulation would not have been feasible. Only parallelization makes it possible to simulate large systems.

4.11 Improved Solid-Wall Boundary Treatment

As a part of this work also solid-wall treatment is studied in Paper 7. In this last part of the thesis, novel discretized equations next to the surface are developed. These equations include new formulae for the velocity derivatives at the wall, for the turbulent stresses in the momentum equation close to the surface, for the production of turbulent kinetic energy in the first computational cell and some other smaller improvements. The proposed methods are applied to a channel flow, a zero pressure gradient boundary layer, the ONERA M6 wing and the BAe Hawk trainer. Although these new methods are applied with one particular turbulence model, Chien's $k - \epsilon$, the most important refinements are directly applicable any eddy-viscosity type approach or with small modifications to the RS models.

For the original model it is shown that the non-dimensional first cell height should have a value less than two, if one percent accuracy is desired in the friction coefficient. Compared to the original modelling, roughly three times larger cells next to the solid boundaries can be used in order to retain the same accuracy. As an example of the new method the results for the flat-plate boundary layer simulation

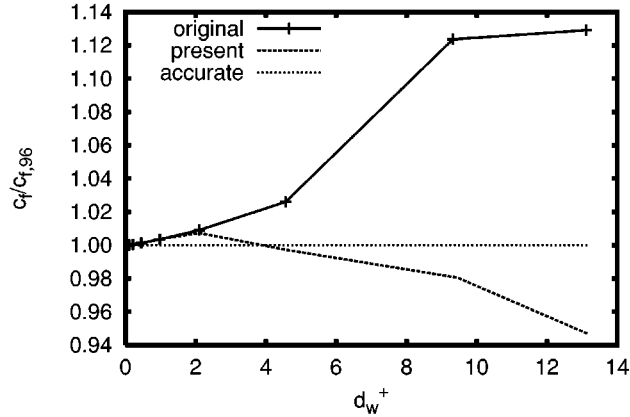


Fig. 4.23: Error in the friction coefficient as a function of cell height (d_w^+) at the location of $Re_x = 800\,000$ for the flat-plate boundary layer.

(same case as in Section 4.3) is presented in Fig. 4.23. In the figure d_w^+ is the height of the first cell next to the surface. The new method clearly improves the results when $2 < d_w^+ < 13$. Accuracy is still very good at the value of the non-dimensional height $d_w^+ = 7$. Similar results are obtained with the ONERA M6 wing and the BAe Hawk trainer in the Paper 7.

4.12 Summary of the Validations

The present Reynolds-stress model overpredicts the skin friction. This can be clearly seen already in the boundary layer case. In two-dimensional flows without rotation, the RSM and EARSM do not work any better than the eddy-viscosity models. This is seen in the channel, the boundary layer and in the wall jet flows. In those cases the eddy-viscosity assumption performs even better in some respect. However, if the flow is three-dimensional, the RSM seems to predict the overall flow field better. This is especially true for the cross-flow components. This can be seen in the cube and the matrix of cubes flows. In addition, in the return channel, the tangential components are better predicted by the RSM. The EARSM generally predicts three-dimensional flows better than eddy-viscosity models, but not as well as the RSM.

In the flows with large separations, the steady-state Reynolds-averaged Navier–Stokes (RANS) equations do not seem to be an appropriate method. These flows are usually time dependent, and thus, the steady-state RANS cannot predict the vortex shedding like phenomena. It could be that when the time-dependent eddies are of the size of the characteristic length of the problem itself, the averaging approach fails. This phenomenon is clearly seen in both cube flows. It could also be one of the reasons why in the return channel flow, the velocity distribution in the shroud is not well captured (Fig. 4.15). In the return channel the real flow field pulsates because

of the rotor. In the simulation, the averaged velocities from the measurement were used.

In order to take into account the rotational effects one must use a method sensitive to rotation. However, only the RSM is able to capture the trend of skin friction in the rotating channel correctly. Although the RSM captured the rotating effects better in the rotating channel flow, it does not seem to bring anything new in the NASA low-speed compressor. Thus, in turbomachinery if there is no large separation, a turbulence does not seem to play an important role in predicting the total values or the velocity distributions. In rotating turbomachinery, the driving forces are much stronger than the turbulent forces, and thus, the turbulence model is not so important. However, the situation at an off-design point could be different. In the diffuser, where the history effects caused by the impeller are important, the RSM predicts better velocity profiles.

5 Conclusions

In this thesis, the validation of different types of turbulence models in various turbulent flows is presented. Turbulence is modelled using a traditional engineering approach, i.e. by time averaging the fluctuations. The turbulent forces are taken into account by using the Reynolds stresses. A new Reynolds-stress turbulence closure is developed as a combination of existing methods parameterized by the author.

Most of the validation cases were simulated with three alternatives: Chien's two-equation model, an explicit algebraic Reynolds-stress model, and the full Reynolds-stress closure. The Reynolds-stress model uses the ideas from Chien's $k - \varepsilon$ model, Shima's RSM, and the RSM by Speziale *et al.* The dissipation equation is taken from Chien's model, the low-Reynolds number part of the dissipation tensor and the pressure-strain tensor are based on Shima's work. The high-Reynolds number modelling of the pressure strain tensor was originally developed by Speziale *et al.*

New numerical methods are developed to couple the momentum equations and the low-Reynolds number Reynolds-stress equations. A novel anisotropic coupling of the Navier–Stokes and the Reynolds-stress equations is introduced. Coupling between the momentum equation and the Reynolds stresses is made possible by using the production term. In the evaluation of the fluxes, the turbulence equations are coupled with the inviscid part of the Reynolds-averaged Navier–Stokes equations, and thus, it is feasible to use Roe's method. For the turbulence quantities, the second-order upwind scheme is applied with a limiter which was found to enhance the robustness of the scheme. The discretized equations are solved using an implicit method with a multigrid acceleration for convergence. In the Reynolds-stress and $k - \varepsilon$ equations, the source term is linearized in a simplified manner. In addition, the limitation of the Reynolds stresses was found to be essential in order to simulate difficult tasks. These methods are proven to be numerically stable and they have a fast convergence rate.

In order to be able to compute large cases, the parallelization is an important tool to reduce computing times. In most of the present simulations the parallel processing has shortened the computing time from the level of a week to the level of a day. The performance of the parallelization is perfect with the "academic" cases and it is still very good with real, complex topologies like with a reactor core.

In complex geometries with a streamline curvature, the simulation of 3-D effects and flow separation often fails with the $k - \varepsilon$ model. This is due to the isotropic Boussinesq approximation as well as the history effect of Reynolds stresses. Generally, the best results for the 3-D cases are achieved by the RSM, although there

are some locations where the situation is not so clear. The cross-flow is generally better captured by the RSM. In simpler 2-D cases, the two-equation models perform generally better. In the flows that contain large time-dependent vortices, like vortex shedding behind the cube, the Reynolds-averaged Navier–Stokes equations might not be an appropriate tool. The problem arises from what time-dependent behaviours, like turbulent fluctuation, should be taken into account by the turbulence model and which part should be solved in flow equations. The difference between the turbulent scales and the main flow scales is vague in this and many similar cases.

One of the biggest shortcomings of the RSM is still the modelling of the wall proximity effects. In the present model, the skin friction is systematically over-predicted. The promising elliptic relaxation method was tested in a simple rotating channel flow. Although the results were good, the generalization of the method is not possible without further development. The boundary conditions in the curvilinear coordinates are not fully evaluated. In the literature, there is a large number of different ideas to take account of the wall proximity effects, but none of them has had extensive validation for complex flows.

The Reynolds-stress model has been the promising future method for over 25 years now. In principle, it contains more information about the turbulent forces than the simpler approaches. Moreover, it includes the anisotropy of these forces, by taking separately into account the production and the history of each Reynolds-stress term. However, the complexity of the unknown source terms might bring too much uncertainty to the model. The use of the RSM requires a specialist to define the boundary conditions and to get reasonable results. Nevertheless, in some complex flows it brings more information about the flow. In order to model turbulence successfully it requires skill, knowledge of the model, an understanding of fluid dynamics, and experience. This is true for all turbulent models, and especially true for the Reynolds-stress model. There is no universal law of turbulence.

Bibliography

- [1] J.O. Hinze. *Turbulence*. McGraw-Hill, New York, 2 edition, 1975. ISBN 0-07-029037-7.
- [2] H. Schlichting. *Boundary Layer Theory*. McGraw-Hill Book Co., New York, 7th edition, 1979. ISBN 0-07-055334-3.
- [3] J. Kim, P. Moin, and R. Moser. Turbulence Statistics in Fully Developed Channel Flow at Low Reynolds Number. *Journal of Fluid Mechanics*, Vol. 177, pp. 133–166, 1987.
- [4] A. Favre. Equations des Gaz Turbulents Compressibles. *Journal de Mécanique*, Vol. 4, No. 3, pp. 361–390, 1965.
- [5] D.A. Anderson, J.C. Tannehill, and R.H. Pletcher. *Computational Fluid Mechanics and Heat Transfer*. Hemisphere Publishing Corporation, New York, 1984. ISBN 0-89116-471-5.
- [6] T. Siikonen. An Application of Roe’s Flux-Difference Splitting for the $k - \epsilon$ Turbulence Model. *International Journal for Numerical Methods in Fluids*, Vol. 21, No. 11, pp. 1017–1039, 1995.
- [7] D. Vandromme. Turbulence Modeling for Turbulent Flows and Implementation in Navier–Stokes Solvers. In *Introduction to the Modeling of Turbulence*. von Karman Institute for Fluid Dynamics Lecture Series 1991-02, 1991.
- [8] P. Rautaeimo, E. Salminen, and T. Siikonen. Numerical Simulation of the Flow in the NASA Low-Speed Centrifugal Compressor. Report 119, Helsinki University of Technology, Laboratory of Applied Thermodynamics, 1998. ISBN 951-22-4360-1.
- [9] B.S. Baldwin and H. Lomax. Thin Layer Approximation and Algebraic Model for Separated Turbulent Flows, Jan 1978. AIAA Paper 78-257.
- [10] F.H. Harlow and P.I. Nakayama. Transport of Turbulence Energy Decay Rate. Technical Report LA-3854, Los Alamos Sci.Lab., University of California, 1968.
- [11] B.E. Launder and B. Spalding. *Mathematical Models of Turbulence*. Academic Press, New York, 1972.

- [12] W.P. Jones and B.E. Launder. The Prediction of Laminarization with a Two-Equation Model of Turbulence. *International Journal of Heat and Mass Transfer*, Vol. 15, pp. 301–314, 1972.
- [13] D.C. Wilcox. Reassessment of the Scale-Determining Equation for Advanced Turbulence Models. *AIAA Journal*, Vol. 26, No. 11, pp. 1299–1310, 1988.
- [14] T.B. Gatski and C.G. Speziale. On explicit algebraic stress models for complex turbulent flows. *Journal of Fluid Mechanics*, Vol. 254, pp. 59–78, 1993.
- [15] S.S. Girimaji. Fully Explicit and Self-Consistent Algebraic Reynolds Stress Model. *Theoretical and Computational Fluid Dynamics*, Vol. 8, pp. 387–402, 1996.
- [16] K.-Y. Chien. Predictions of Channel and Boundary-Layer Flows with a Low-Reynolds-Number Turbulence Model. *AIAA Journal*, Vol. 20, No. 1, pp. 33–38, 1982.
- [17] N. Shima. A Reynolds-Stress Model for Near-Wall and Low-Reynolds-Number Regions. *Journal of Fluids Engineering*, Vol. 110, pp. 38–44, 1988.
- [18] C.G. Speziale, S. Sarkar, and T.B. Gatski. Modelling the pressure-strain correlation of turbulence: an invariant dynamical systems approach. *Journal of Fluid Mechanics*, Vol. 227, pp. 245–272, 1991.
- [19] V.C. Patel, W. Rodi, and G. Scheuerer. Turbulence Models for Near-Wall and Low Reynolds Number Flows: A Review. *AIAA Journal*, Vol. 23, No. 9, pp. 1308–1319, 1985.
- [20] R. Abid, C. Rumsey, and T.B. Gatski. Prediction of Nonequilibrium Turbulent Flows with Explicit Algebraic Stress Models. *AIAA Journal*, Vol. 33, No. 11, pp. 2026–2031, 1995.
- [21] B. E. Launder, G. J. Reece, and W. Rodi. Progress in the Development of a Reynolds-Stress Turbulence Closure. *Journal of Fluid Mechanics*, Vol. 68, pp. 537–566, 1975.
- [22] L. Davidson and A. Rizzi. Navier–Stokes Stall Predictions Using an Algebraic Reynolds-Stress Model. *Journal of Spacecraft and Rockets*, Vol. 29, No. 6, pp. 794–800, 1992.
- [23] F.S. Lien and M.A. Leschziner. A General Non-orthogonal Collocated Finite Volume Algorithm for Turbulent Flow at all Speeds Incorporating Second-Moment Turbulence-Transport Closure, Part 1: Computational Implementation. *Computer Methods in Applied Mechanics and Engineering*, Vol. 114, pp. 123–148, 1994.
- [24] T. Siikonen, J. Hoffren, and S. Laine. A Multigrid *LU* Factorization Scheme for the Thin-Layer Navier–Stokes Equations. In *Proceedings of the 17th ICAS Congress*, pp. 2023–2034, Stockholm, Sept. 1990. ICAS Paper 90-6.10.3.

- [25] P.L. Roe. Approximate Riemann Solvers, Parameter Vectors, and Difference Schemes. *Journal of Computational Physics*, Vol. 43, No. 2, pp. 357–372, 1981.
- [26] A.J. Chorin. A Numerical Method for Solving Incompressible Viscous Flow Problems. *Journal of Computational Physics*, Vol. 2, pp. 12–26, 1967.
- [27] C.K. Lombard, J. Bardina, E. Venkatapathy, and J. Oliger. Multi-Dimensional Formulation of CSCM — An Upwind Flux Difference Eigenvector Split Method for the Compressible Navier–Stokes Equations. In *6th AIAA Computational Fluid Dynamics Conference*, pp. 649–664, Danvers, Massachusetts, Jul 1983. AIAA Paper 83-1895-CP.
- [28] A. Jameson and S. Yoon. Multigrid Solution of the Euler Equations Using Implicit Schemes. *AIAA Journal*, Vol. 24, No. 11, pp. 929–935, 1986.
- [29] G.D. Van Albada, B. Van Leer, and W.W. Roberts. A Comparative Study of Computational Methods in Cosmic Gas Dynamics. *Astronom. and Astrophys.*, Vol. 108, No. 76, pp. 76–84, 1982.
- [30] P. Rautahaimo and T. Siikonen. Numerical Methods for Coupling the Reynolds-averaged Navier–Stokes Equations with the Reynolds-stress Turbulence Model. Report 81, Helsinki University of Technology, Laboratory of Applied Thermodynamics, 1995. ISBN 951-22-2748-7.
- [31] S. Obayashi and K. Kuwahara. An Approximate LU Factorization Method for the Compressible Navier–Stokes Equations. *Journal of Computational Physics*, Vol. 63, No. 1, pp. 157–167, March 1986.
- [32] J.L. Lumley. Computational Modeling of Turbulent Flows. In *Advances in Applied Mechanics*, volume 18, pp. 123–176. Academic Press, 1978. ISBN 0-12-002018-1.
- [33] G. Bärwolff, K. Ketelsen, and F. Thiele. Parallelization of a Finite-Volume Navier–Stokes Solver on a T3D Massively Parallel System. In *Sixth International Symposium on Computational Fluid Dynamics*, Lake Tahoe, Nevada, Sept. 1995.
- [34] M.L. Sawley and J.K. Tegner. A Comparison of Parallel Programming Models for Multiblock Flow Computations. *Journal of Computational Physics*, Vol. 122, pp. 280–290, 1995.
- [35] Message Passing Interface Forum. MPI: A Message-Passing Interface Standard. Technical report CS-94-230, Computer Science Dept., University of Tennessee, Knoxville, TN, 1994.
- [36] P. Rautahaimo, P. Kaurinkoski, and T. Siikonen. Performance of a Parallel CFD-Code on a Linux Cluster. *CSC News*, Vol. 11, No. 4, pp. 19–22, 1999.

- [37] P. Kaurinkoski, P. Rautahaimo, T. Siikonen, and K. Koski. Performance of a Parallel CFD-Code on a Linux Cluster. In J. Periaux A. Ecer and N. Sato-fuka, editors, *Parallel Computational Fluid Dynamics 2000*, Amsterdam, The Netherlands, 2000. Elsevier Science B.V.
- [38] A. Hellsten, P. Rautahaimo, S. Laine, and T. Siikonen. Description of Numerical Methodology for Test Case 7.1. In Craft T.J., editor, *Proceedings of the 7th ERCOFTAC/IAHR Workshop on Refined Flow Modelling*, UMIST, Manchester, UK, May 1998. Unpublished.
- [39] A. Hellsten. On the Solid-Wall Boundary Condition of ω in the $k - \omega$ -Type Turbulence Models. Report B-50, Helsinki University of Technology, Laboratory of Aerodynamics, 1998. ISBN 951-22-4005-X.
- [40] D.C Wilcox. *Turbulence Modeling for CFD*. DCW Industries, Inc., La Canada, 1993. ISBN 0-9636051-0-0.
- [41] A. Hellsten. Some Improvements in Menter's $k - \omega$ SST Turbulence Model. In *29th AIAA Fluid Dynamics Conference*, Albuquerque, New Mexico, USA, 1998. AIAA paper 98-2554.
- [42] P.A. Durbin. A Reynolds stress model for near-wall turbulence. *Journal of Fluid Mechanics*, Vol. 249, pp. 465-498, 1993.
- [43] B.A. Pettersson and H.I. Andersson. Near-wall Reynolds-stress modelling in noninertial frames of reference. *Fluid Dynamics Research*, Vol. 19, pp. 251-276, 1997.
- [44] P. Rautahaimo and T. Siikonen. Improved Solid-Wall Boundary Treatment in Low-Reynolds Number Turbulence Models. Report 122, Helsinki University of Technology, Laboratory of Applied Thermodynamics, Espoo, Finland, 1999. ISBN 951-22-4666-X.
- [45] R.I. Karlsson, J. Eriksson, and J. Persson. LDV Measurements in a Plane Wall Jet in a Large Enclosure. In *6th International Symposium on Applications of Laser Techniques to Fluid Mechanics*, pp. 1.5.1-1.5.6, Lisbon, Portugal, July 1992.
- [46] W.J. Kim and V.C. Patel. Origin and Decay of Longitudinal Vortices in Developing Flow in a Curved Rectangular Duct. *Journal of Fluid Engineering*, Vol. 116, pp. 45-52, March 1994.
- [47] I. Dauthieu, D. Laurence, and S. Richoux, editors. *Proceedings of the 5th ERCOFTAC/IAHR Workshop on Refined Flow Modelling*, Chatou (Paris), France, April 1996. Unpublished.
- [48] W. Rodi, H.J. Ferziger, M. Breuer, and M. Pourquié. Status of Large-Eddy Simulation: Results of a Workshop. *Journal of Fluid Engineering*, Vol. 119, 1997.

- [49] R. Martinuzzi and C. Tropea. The flow around surface-mounted, prismatic obstacles placed in a fully developed channel flow. *Journal of Fluid Engineering*, Vol. 115, pp. 85, 1993.
- [50] A. Hellsten and P. Rautheimo, editors. 8th ERCOFTAC/IAHR/COST Workshop on Refined Turbulence Modelling. Report 127, Helsinki University of Technology, Laboratory of Applied Thermodynamics, Espoo, Finland, 1999. ISBN 951-22-4772-0.
- [51] E.R. Meinders. *Experimental study of heat transfer in turbulent flows over wall-mounted cubes*. PhD thesis, Delft University of Technology, 1998.
- [52] F.R. Menter. Two-Equation Eddy-Viscosity Turbulence Models for Engineering Applications. *AIAA Journal*, Vol. 32, No. 8, pp. 1598-1605, 1994.
- [53] D. Japikse and K. Oliphant. Return Channel, Swirl Generator Rotor and Deswirl Cascade. ERCOFTAC Turbomachinery Workshop Test Case F3, 1998.
- [54] M.D. Hathaway, M.C. Randall, J. Strazisar, and J.R Wood. Laser Anemometer Measurements of the Three-Dimensional Rotor Flow Field in the NASA Low-Speed Centrifugal Compressor. Technical Report Technical Paper 3527, Army Research Laboratory, Cleveland, Ohio, 1995.